The Journal of Undergraduate Research in Physics

CONTENTS

Volume 13, Number 2
May, 1995

Published by the Physics Department of Guilford College
for
The American Institute of Physics and the Society of Physics Students

THE JOURNAL OF UNDERGRADUATE RESEARCH IN PHYSICS

This journal is devoted to research work done by undergraduate students in physics and its related fields. It is to be a vehicle for the exchange of ideas and information by undergraduate students. Information for students wishing to submit manuscripts for possible inclusion in the Journal follows.

ELIGIBILITY
The author(s) must have performed all work reported in the paper as an undergraduate student(s). The subject matter of the paper is open to any area of pure or applied physics or physics related field.

SPONSORSHIP
Each paper must be sponsored by a full-time faculty member of the department in which the research was done. A letter from the sponsor, certifying that the work was done by the author as an undergraduate and that the sponsor is willing to be acknowledged at the end of the paper, must accompany the manuscript if it is to be considered for publication.

SUBMISSION
Two copies of the manuscript, the letter from the sponsor and a telephone number or E-Mail address where the author can be reached should be sent to:

Dr. Rexford E. Adelberger, Editor
THE JOURNAL OF UNDERGRADUATE
RESEARCH IN PHYSICS
Physics Department
Guilford College
Greensboro, NC 27410

FORM
The manuscript should be typed, double spaced, on 8 1/2 x 11 inch sheets. Margins of about 1.5 inches should be left on the top, sides, and bottom of each page. Papers should be limited to fifteen pages of text in addition to an abstract (not to exceed 250 words) and appropriate drawings, pictures, and tables.

Manuscripts may be submitted on a disk that can be read by a MacIntosh™. The files must be compatible with MacWrite™, MicroSoft Word™ , PageMaker™ or WordPerfect™.

ILLUSTRATIONS
Line drawings should be made with black ink on plain white paper. Each figure or table must be on a separate sheet. Photographs must have a high gloss finish. If the submission is on a disk, the illustrations should be in PICT, TIFF or EPS format.

CAPTIONS
A brief caption should be provided for each illustration or table, but it should not be part of the figure. The captions should be listed together at the end of the manuscript

EQUATIONS
Equations should appear on separate lines, and may be written in black ink. We use EXPRESSIONIST™ to format equations in the Journal.

FOOTNOTES
Footnotes should be typed, double spaced and grouped together in sequence at the end of the manuscript.

PREPARING A MANUSCRIPT
A more detailed set of instructions for authors wishing to prepare manuscripts for publication in the Journal of Undergraduate Research in Physics can be found in Volume 8 #1 which appeared in October of 1989 or in Volume 11 #2 which appeared in May of 1993.

SUBSCRIPTION INFORMATION

The Journal is published twice each academic year, issue # 1 appearing in November and issue # 2 in May of the next year. There are two issues per volume.

TYPE OF SUBSCRIBER	PRICE PER VOLUME
Individual	$US 5.00
Institution	$US 10.00

Foreign subscribers add $US 2.00 for surface postage, $US 10.00 for air freight.

Back issues may be purchased by sending $US 15.00 per volume to the editorial office.

To receive a subscription, send your name, address, and check made out to **The Journal of Undergraduate Research in Physics (JURP)** to the editorial office:

JURP
Physics Department
Guilford College
Greensboro, NC 27410

The Journal of Undergraduate Research in Physics is sent to each member of the Society of Physics Students as part of their annual dues.

A CATALOGUE OF SUPERNOVA REMNANT CANDIDATES IN M83

Joseph F. McCullough *
Department of Physics and Astronomy
The Johns Hopkins University
Baltimore, MD 21218
received May 20, 1994

ABSTRACT

Observations of the face-on spiral galaxy M83 (NGC5236) performed at the Cerro Tololo Inter-American Observatory in Chile have yielded a catalogue of supernova remnant candidates (SNR). These observations were performed with the 4 m telescope and a prime focus CCD imaging system using narrow band interference filters centered on the light of [S II], H_α, [O III] and red and blue continuum bands. Based on the strong relative [S II]:H_α emission, 38 emission nebulae have been identified as SNR candidates. Positions, diameters and luminosities of the candidates are presented. We also have attempted to identify optical counterparts for the six historical supernovae that have occurred in M83. Except for the one reported previously, none of the historical supernovae have been detected by this survey.

INTRODUCTION

The luminosity of a supernova (SN) is comparable to that of an entire galaxy. This intense light, however, fades quickly and most optical supernovae (SNe) disappear within a year or less. As the shock wave from the exploded star interacts with the circumstellar and interstellar medium (ISM), the luminosity once again rises in what is now called a supernova remnant (SNR). For a SNR to become bright enough to detect optically, the expanding blast must encounter relatively dense circumstellar material. The evolution of a SNR consequently depends heavily on the density and composition of the surrounding medium. It often takes thousands of years after a star explodes before we see a SNR. These remnants in turn can affect the ISM. They provide substantial energy input (typically 10^{44} J/SN) and return processed material back to the ISM.

The study of young SNRs (before they have sufficiently interacted with the surrounding material) is important because it provides information on the final evolutionary stages of the progenitor star (e.g. mass and composition). The study of large samples of SNR's in a galaxy can be used to investigate global properties of the galaxy's ISM and SNR evolution. It also can give a rough estimate of the SN rate, which can in turn be used to determine the structure, kinematics and composition of the ISM. [1] The study of SNRs in our own galaxy is difficult because of uncertain distances to individual objects and the high extinction along the line of sight. Extragalactic SNR studies are advantageous in that all SNRs in the sample are at almost the same distance away, and hence can be compared directly. It has been shown [1] that SNe (and consequently their remnants) are more difficult to detect in galaxies that are nearly edge-on ($i > 60°$), affecting estimates of the actual SN rate in these galaxies. By studying galaxies that are nearly face-on, the effects of extinction can be minimized.

Extragalactic searches for SNRs were pioneered by Mathewson and Healy in 1964 [2] and then by Mathewson and Clark in 1973 [3]. They used the fact that the optical spectra of SNRs have elevated [S II]:H_α emission line ratios as compared to the spectra of normal H II regions. This emission ratio has been shown to be an accurate means of differentiating between shock heated SNRs (ratios > 0.40) and photoionized nebulae (ratio < 0.40). The physical basis for this is that in typical H II regions, sulfur exists mainly in the form S^{++}, yielding low [S II] ($\lambda = 6717$Å, 6731Å) to H_α emission ratios ≈ 0.10. After the shock wave from a SN explosion has propagated through the surrounding medium and the material has cooled sufficiently, a variety of ionization states are present, including S^{+}. This accounts for the increased [S II]:H_α (ratio > 0.4) emission observed in SNRs. Spectroscopic observations of such emission nebulae usually provide other evidence of shock heating, verifying the candidate to be an SNR. [4,5,6,7] Thus, we have a

Joe graduated from Johns Hopkins University in 1992 with a major in physics. Since that time, he has been teaching physics at Trinity-Pawling School in upstate New York. During his spare time, Joe is an outdoor enthusiast and is an avid mountain climber. He hopes to attend graduate school next year.

SN Note	R.A (1950)	Decl. (1950)	Type	
1923a	13h34m20.0s	-29°34'19.5"	II	1
1945b	13 34 04.0	-29 39 39.4	--	2
1950b	13 34 03.8	-29 36 40.5	--	3
1957d	13 34 14.3	-29 34 24.0	II	3
1968l	13 34 11.2	-29 36 42.2	II	2
1983n	13 34 01.7	-29 38 48.0	I	3

1) Position from (ref 22).
2) Positions of SN1945b (only recently discovered from archival data (ref 23) and SN198l (ref 24) are given in terms of an off-set from galactic center. We have used R.A (1950) = 13h34m11.55s, Dec.(1950) = -29°36'42.2" (ref 9) as the galactic center's coordinates.
3) Positions are taken from a 1985 radio search of M83 (ref 25).

Table 1
Information on Historical SNe in M83

powerful method of identifying SNRs in nearby galaxies.

This was the method employed in our search of M83, classified by astronomers as a SAB(s)c galaxy, to indicate the its shape, at a distance of 3.75 Mpc.[8] It is the most distant galaxy for which a SNR survey has been attempted to date. M83 is at an inclination angle of 24 degrees [9] and has an angular size of approximately 13 arcminutes (a value derived from the apparent isophotal diameter [10]). It has well formed spiral arms and distinct dust lanes as seen in Figure 1. Detailed observations at radio [11], infrared [12], ultraviolet [13], X-ray [14], and optical wavelengths [15] indicate that the nucleus of M83 is a region of intense star formation. Absorption features [15] were found that were consistent with a population dominated by massive OB stars, which are believed to be the precursors of Type II SNe [16]. Observations show a large number of young, massive stars along the inner arms, indicating active star formation in these regions as well. [17] These observations are consistent with other evidence [14] for a recent burst of star formation occurring about 10^7 years ago. This ubiquitous star formation makes M83 a natural target for SNR studies.

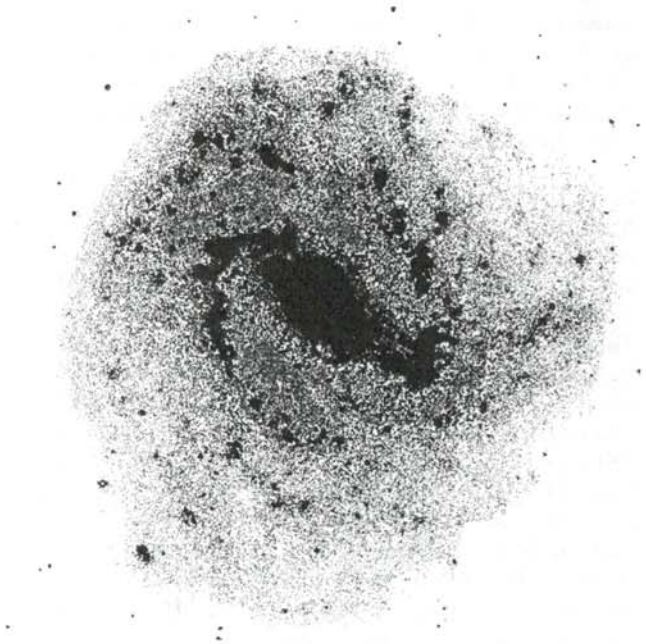

Figure 1
Image of M83 observed through the H_α filter. The NW, CTR and SE images have been combined.

We also conducted an optical search for the six historical (previously seen) SNe which have occurred in M83. [18] Information on these SNe are given in Table 1. Only one other galaxy, NGC 6946 has had a comparable number of historical SNe. This large SN rate provides an excellent opportunity to investigate the early stages of SNR evolution, as there should be numerous other young SNR's between 100 and 1000 years old present in M83.

OBSERVATIONS AND DATA REDUCTIONS

The observations of M83 were performed with the 4 m telescope of the Cerro Tololo Inter-American Observatory in Chile. Three fields of M83 were observed using a 1024 x 1024 pixel CCD on April 18 and 19, 1991. The three fields (NW, SE and CTR) were each approximately 8′ in extent with the central 4.8′ x 4.4′ region of M83 being covered by all three fields (see Figure 1). Centers for the three fields are given in Table 2, along with the scale and rotation angle. Plate solutions , an astrometric function that links pixel positions to coordinates on the sky, for these fields were derived from astrometry performed on digitized GSC Palomar Sky Survey J Plates. The solutions obtained were of 0.27 arcsec RMS residual accuracy. We used narrow band interference filters centered on the lines of [S II], H_α, [O III] and a portion of the red and blue continuum isolated from emission lines. The central wavelength and width of each filter as well as exposure times are listed in Table 3. Three exposures were made with each filter for each field.

The data were reduced using the Interactive Reduction and Analysis Facility (IRAF) software developed and distributed by the National Optical Astronomy Observatories. The three exposures of each field through each filter were combined to reduce the effect of cosmic rays and increase

Field	R.A. [a] (1950)	Dec. [a] (1950)	Derived Scale ("/pixel)	Rot. angle[b] (degrees)
NW	13h34m03.62s	-29°35' 01.3"	0.4708	1.175
CTR	13 34 10.46	-29 36 34.5	0.4706	1.175
SE	13 34 18.54	-29 38 32.5	0.4701	1.183

[a] *Positions refer to the field center*
[b] *Rotation angle of CCD columns with respect to North*

Table 2
Plate solutions for the three fields.

the signal-to-noise ratio for the faintest objects. Each exposure was bias subtracted, trimmed and flat fielded (to remove pixel to pixel variations) before being combined. Observations of spectrophotometric standard stars [19] were used to determine the flux conversion and the amount of background to be subtracted for each night. LTT3864, LTT6248 and LTT7379 were used on 18 April and LTT3864 was used on 19 April. By comparing the observed count rate received on each night through each filter with the actual flux (in J/m^{2}s) over the band pass of each filter from the standard stars, an accurate count rate to flux conversion was established. The results of each observation were consistent to within 10%. The effective seeing on 18 April (1.5") was slightly better than on 19 April (1.7"). The arcsecond values indicate the effective seeing on each night; 1.5" means that a point-like object (a star) would appear to have a width of 1.5" because of atmospheric seeing. For the assumed distance of 3.75 Mpc, 1" corresponds to a linear scale of 18.2 pc.

IDENTIFICATION OF CANDIDATES

To identify the SNR candidates in M83, we used a method of blinking and measuring the [S II], H_α and red continuum images on an interactive image display on a workstation. An image with regions of [S II]:H_α emission > 0.3 blacked out, superimposed on the H_α image, was also used to highlight possible SNR candidates. This is shown in Figure 2.

To blink the images, we first separated each of the three regions into 25 smaller regions of about 2 arcminutes on a side. These images then had the background subtracted for each filter. The red continuum filter, centered at 6826Å provided an accurate background subtraction. Because the workstation could only view one image at a time, we used a method of 'blinking' the images in rapid succession to find regions of elevated [S II:H_α] emission which did not have a corresponding continuum emission,

Nebulae with [S II]:H_α emission ratios > 0.4 were flagged as possible candidates. This elevated emission must be accompanied by a corresponding absence of continuum emission, which can contribute equally in each filter and give an artificially high ratio.

While this is an effective method for identifying large, isolated regions of high [S II]:H_α emission, smaller and more complicated regions can be harder to identify. At a distance of 3.75 Mpc, each pixel in the CCD corresponded to a distance of 8.5 pc. The smallest SNR candidate identified was approximately 27 pc in diameter, limited by the seeing for each night. Candidates with H_α emission, (above the background) less than 2×10^{-13} (J/m^{2}s) were not considered. It was too difficult to systematically establish any structure against the background at such low flux levels.

Filter	Central Wavelength (Å)	FWHM (Å)	Exposure Time (seconds)
[S II]	6719	50	600
H_α	6560	52	600
[O III]	5020	54	600
Red Cont.	6826	85	400
Blue Cont.	5125	44	500

Table 3

Interference filter characteristics and times for exposures using the various filters.

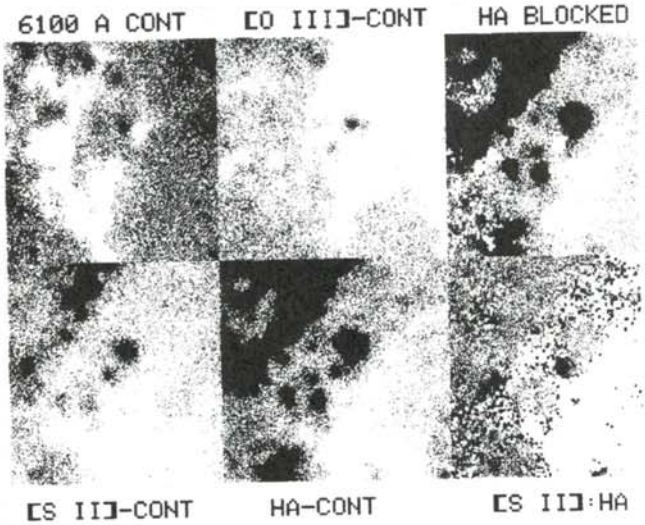

Figure 2

Images of SNR candidate at R.A.(1950)=13^{h}34^{m}18.14^s, Dec.(1950)=-29°36'14.2" (located in the center of each sub-image) observed through the red continuum filter (upper left), the [O III] filter (upper middle), the [S II] filter (lower left) and the H_α filter (lower middle). The upper right image has regions with [S II]:H_α emission ratio > 0.30 blacked out superimposed over the H_α image. This image was used to draw attention to a possible SNR candidate. The lower right image is a ratio image using continuum substracted sub images of [S II] and H_α. Regions of high relative [S II]:H_α line emission appear darker. This image was used to determine the boundaries of some SNR's which were located in regions with relatively complex backgrounds or in H II regions.

When searching for the historical SNe in M83, we used a blue filter, centered at 5125Å for continuum subtraction. This was done because of its proximity to the center of the [O III] filter. Nebulae with high [O III]:H_α emission can result from the explosion of a massive progenitor star. Several of the historical SNe were either observed or inferred to be of Type II, indicating a massive star as the likely precursor.

RESULTS

While many observations of M83 have been made at all wavelengths, this is the first optical search for SNRs performed. The method of blinking the images proved effective in identifying a large group of nebulae which,

(1) R.A. (1950)	(2) Dec. (1950)	(3) Diameter	(4) Mean [S III] Surface Brightness [a]	(5) Mean H_α Surface Brightness [b]	(6) [S II]:Ha	(7) Group [c]
13h	-29°	(pc)	x10-12(J/m2s)			
34m29.41s	38'31.9"	34	0.2	0.4	0.51	1
34 28.20	38 17.2	30	0.1	0.2	0.55	2
34 27.93	38 06.5	43	0.6	1	0.50	1
34 25.55	39 39.9	43	1	2	0.44	3
34 25.11	35 03.2	43	0.3	0.6	0.41	2
34 25.01	34 48.2	30	0.1	0.2	0.56	2
34 24.64	36 32.8	43	0.4	0.8	0.56	1
34 22.34	36 21.6	≤ 27	0.2	0.4	0.56	1
34 22.17	36 23.1	34	0.4	0.7	0.62	2
34 21.49	36 26.6	43	0.3	0.7	0.47	2
34 18.58	38 54.7	51	0.3	0.7	0.44	2
34 18.33	37 00.8	43	0.3	0.6	0.53	2
34 18.23	38 58.1	34	0.2	0.3	0.65	2
34 18.15	36 15.2	51	0.1	0.3	0.45	1
34 17.70	33 49.9	60	1	2	0.57	3
34 17.14	35 07.2	43	0.9	2	0.43	3
34 17.11	34 48.9	38	0.2	0.5	0.43	2
34 17.20	39 09.2	34	0.2	0.6	0.42	1
34 16.67	34 46.2	≤ 27	0.3	0.4	0.74	2
34 15.48	34 49.3	34	0.3	0.4	0.70	2
34 12.90	34 34.5	34	0.6	2	0.42	1
34 12.81	36 41.2	38	0.7	1	0.66	2
34 12.21	34 57.3	34	0.2	0.4	0.51	1
34 11.94	41 52.7	43	0.3	0.5	0.48	1
34 11.74	35 38.4	≤ 27	0.1	0.3	0.45	1
34 11.02	36 03.0	30	0.2	0.4	0.63	2
34 10.07	33 59.0	43	0.3	0.6	0.54	3
34 10.22	36 46.1	30	0.4	0.6	0.72	2
34 07.91	38 16.1	43	0.3	0.6	0.42	1
34 06.07	33 21.9	38	0.3	0.8	0.41	3
34 06.20	37 26.2	34	0.6	1	0.55	2
34 06.23	37 46.0	≤ 27	1	3	0.42	1
34 04.89	36 51.7	34	0.3	0.8	0.42	1
34 04.37	37 28.6	43	0.6	1	0.55	2
34 03.09	35 26.5	38	0.2	0.4	0.46	1
33 59.29	36 48.5	60	1	2	0.5	1
33 57.96	33 47.2	≤ 27	0.2	0.5	0.42	3
33 51.61	36 01.2	30	0.3	0.5	0.56	1

a Values for the [S II] flux were derived using a count-to-flux conversion of 2.465x10-16(J/m2s)
b values for the H_α flux were derived using a count-to-flux conversion of 3.546x10-16(J/m2s)
c See text for description of groups

Table 4
M83 SNR candidates

based on [S II]:H_α emission >0.4, are almost certainly SNRs. The results of our search are presented in Table 4. Columns 1 and 2 give the positions of the SNR candidates in 1950 coordinates. These positions were obtained using a centering algorithm on the H_α images, or in a few cases, the [S II] image. Column 3 lists the diameter for each candidate. The diameters listed are for the greatest dimension in the cases where the candidate was not circular. The accuracy varies because in many cases, the SNR candidate was not well-defined. Columns 4 and 5 give the mean surface brightness for the [S II] and H_α images respectively. The accuracy of these values varied depending on non-uniformities in the background and whether the SNR candidate was located in or around an H II region. Column 6 lists the [S II]:H_α emission ratios. Column 7 gives comments on each of the candidates.

As numerous candidates were identified, they were grouped into three categories:

1. where they are isolated and have a distinct circular shape. Each candidate is well enough defined that the diameters measured are reasonably accurate. The backgrounds are uniform, giving accurate values for the mean surface brightnesses and ratios. Any nebulae listed in this category should be considered an excellent SNR candidate.
2. where candidates had irregular shapes, making the determination of diameter difficult. The diameters in many cases may be over estimates. The positions should be within 2 arcseconds of the actual position. The uncertain positions may have affected the mean surface brightness values in some cases, which in turn would have affected the ratios determined.
3. where the candidates were located in or in close proximity to H II regions. This made the background subtraction uncertain, giving inaccurate surface brightness for the H_α images. In most cases, the [S II] emission was well defined, giving good values for the mean surface brightness. Positions and diameters for these candidates were taken from the [S II] image.

A plot of all the SNR candidates, projected onto the center field of M83, is given in Figure 3. M83 is shown in the observer's reference frame and has not been corrected for inclination effects. When corrected for inclination effects, the number of SNRs/kpc2 decreases steadily with distance from the nucleus of the galaxy. It becomes zero at a radius of 6 kpc. This is likely a result of the active star formation occurring within the nucleus and the inner spiral arms.

With the exception of SN1957d, we were unable to detect optical counterparts for the historical supernovae which have occurred in M83. SNe 1923a, 1945b, 1950b, 1968l and 1983n could not be identified in the light of [S II], [O III] or H_α. This absence of optical nebulae at the positions of the historical SNe implies that the explosions had occurred in relatively low density surroundings. This might be expected if the massive progenitor stars swept out a cavity in the ISM surrounding the supernovae.

We did, however, optically identify SN1957d in the light of [O III]. SN1957d was first discovered as a source of [O III] emission in 1987 [20], making it the first extragalactic historical SN unambiguously detected at optical wavelengths. We detected a mean [O III] surface brightness of about 1 x 10-13 (J/m2s). This is a dramatic decrease from the previous value observed. [21] Continued observations of SN1957d will prove valuable in determining the evolution of young supernovae.

Although the identified SNR candidates have to be verified by spectroscopic observations to confirm the large [S II]:H_α ratios derived from the imagery and search for other evidence of shock heating such as strong [O I] emission and/or high [O III] electron temperatures, we can be confident that the candidates presented here are SNRs based upon their elevated [S II:H_α] emission. This list is by no means complete, our survey was limited by the complexity of M83's background. Any SNRs buried in H II regions or hidden behind dust lanes could not be detected by this survey. With 5 SNe observed since 1923, M83 has an implied supernova rate of approximately one SN every 10 years. The total number of SNRs in M83

should be immense. Although continued observations of M83 are necessary to further study these remnants and how they evolve, the results of this study are encouraging. Our survey is the second largest sample of optical SNRs known; only M33 has a larger number. [6,7] We have shown that optical techniques used on nearby galaxies are effective for identifying a significant sample of SNR's, even at a distance of 3.75 Mpc.

ACKNOWLEDGMENTS

The author would like to thank Dr. William P. Blair for his sponsorship of this paper and for his generous support and assistance during all aspects of this project.

REFERENCES

* current address of the author: Trinity-Pawling School, 300 Route 22, Pawling, NY 12564.
1. S. van den Bergh and G. Tammann, Ann. Rev. Astron. Astrophys., 29, (1991), p. 363.
2. D.S. Mathewson and J.R. Healy, in IAU Symposium 20, The Galaxy and the Megallanic Clouds, ed F.J. Kerr and A.N. Rodger, Australia Academy of Sciences, Canberra, (1964).
3. D.S. Mathewson and J.N. Clarke, Ap. J., 180, (1973), p. 725.
4. W.P. Blair, R.P. Kirshner and R.A. Chevalier, Ap. J. 247, (1989), p. 879.
5. W.P. Blair, R.P. Kirshner and R.A. Chevalier, Ap. J., 254, (1982), p. 50.
6. K.S. Long, W.P. Blair, R.P. Kirshner and P.F. Winkler, Ap. J. Suppl., 72, (1990), p. 62.

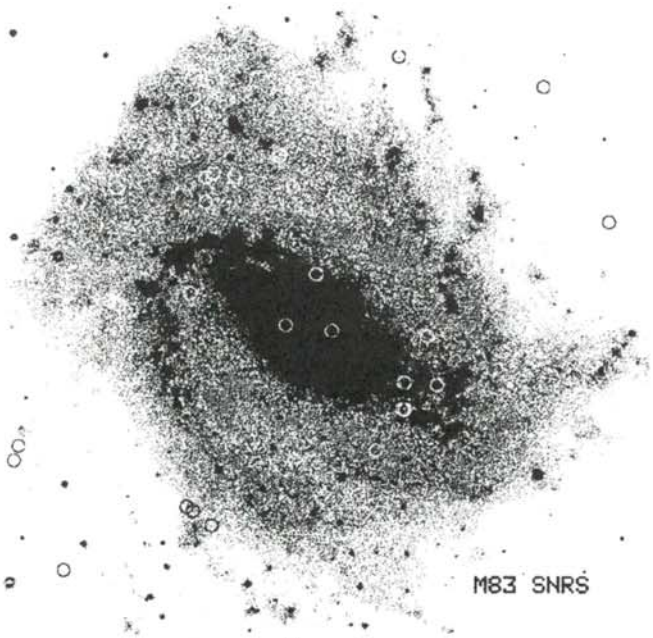

Figure 3
A plot of SNR candidates projected onto the center field of M83. The image was taken using the [S II] filter, but has not had continuum emission subtracted.

7. R.C. Smith, R.P. Kirshner, W.P. Blair, K.S. Long and P.F. Winkler, Ap. J., 407, (1993), P. 564.
8. G. de Vaucouleurs, Ap. J., 84, (1979), p. 1270.
9. R.J. Talbot, Jr., E.B. Jensen and R. Dufour, Ap. J., 229, (1979), p. 91.
10. G. deVaucouleurs, A. de Vaucouleurs, H.G. Corwin, Jr., R.J. Buta, G. Paturel and P. Fouque, Third Reference Calatogue of Bright Galaxies, (1991).
11. J.J. Condon, M.A. Condon, G. Gisler and J.J. Puschell, Ap. J., 252, (1982), p. 102.
12. C.M. Telesco and D.A. Harper, Ap. J., 235, (1980), p. 392.
13. R.C. Bohlin, R.H. Cornett, J.K. Hill, A.M. Smith and T.P. Stecher, Ap. J. (Letters), 274, (1983), p. 153.
14. G. Trinchieri, G. Fabbiano and G.G.C. Palumbo, Ap. J., 290, (1985), p. 96.
15. S. D'Odorico, M. Pettini and D. Ponz, Ap. J., 299, (1985), p. 852.
16. Y.I. Huang, Pub. Astron. Society of the Pacific, 99, (1987) p. 461.
17. E.B. Jensen, R.J. Talbot, Jr. and R.J. Dufour, Ap. J., 243, (1981), P. 716.
18. R. Barbon, E. Cappellaro and M. Turatto, A. , A. J., 81, (1989), p. 421.
19. J.A.Baldwin and R.P.S. Stone, Monthly Notices of the Royal Astron. Society, 206, (1984), p. 241.
20. K.S. Long, W.P. Blair and W. Krzeminski, Ap. J. (Letters), 340, (1987), p. L25.
21. K.S. Long, P.F. Winkler and W.P. Blair, Ap. J. (Letters), 395, (1992), p. 632.
22. R.L. Pennington, R.J. Talbot, Jr., and R. Dufour, Ap. J., 87, (1982), p. 1538.
23. IAU circular 5091.
24. R. Barbon, E. Cappellaro, F. Ciatti, M. Turatto and C.T. Kowal, Astr. Ap. Suppl., 58, (1984) p. 735.
25. J.J. Cowan and D. Branch, Ap. J. 293, (1985), p. 400.

FACULTY SPONSOR

Dr. William P. Blair
Center for Astrophysical Sciences
Bloomberg Center for Physics and Astronomy
The Johns Hopkins University
3400 N. Charles Street
Baltimore, MD 21218-2695

OPTICAL FLOW AS A DETERMINATION OF PARTICULATE FLOW VELOCITY

Ryan Newcomer * and Ben Hanson **
Physics Department
Loyola College
Baltimore, MD 21210
received June 13, 1994

ABSTRACT

Optical flow is a computational technique used on successive images to determine the two-dimensional velocity field of moving objects. We applied these techniques to particulate fluid flows. To evaluate the effectiveness of the technique, we tested algorithms on simulated uniform flow data, experimental data of a single particle and multiparticle flow through a glass capillary. Excellent qualitative velocity maps were obtained. With some interpretation, optical flow yielded good quantitative information.

INTRODUCTION

An interest exists in understanding and measuring the velocity distribution in particulate flows. To accomplish this, one finds a velocity vector associated with each particle. If there are many particles present, calculating the velocity vector for each of the particles produces a velocity vector field representing the motion of the flow.

One example of particulate flow is blood moving through the venules and arterioles of the human body. The flow has been measured in a number of ways: cell tracking; the streak method, using a moving prism to follow a red blood cell; dual-slit, dual-window and spatial correlation methods which examine two points on the capillary and correlate the data to find a displacement; and many other techniques. All the techniques, other than cell tracking, only measure the velocity of the overall flow, not the two-dimensional flow field.[1]

One difficulty in particle tracking is the identification of individual objects. In this paper, we apply the method of optical flow to a series of digital images to calculate the velocity at each pixel by examining the change in the brightness field. The optical flow algorithms offer a way of measuring the velocity of the flow at each pixel without the need of tracking individual objects.

THE HORN AND SCHUNCK ALGORITHM

Objects moving in front of a camera produce a series of changing images. The motion field is the two-dimensional projection of this motion into the focal plane of the camera. A velocity vector can be associated with each point. The brightness pattern is the pixel intensity value at each point in the image. Optical flow is the movement of the brightness patterns through a series of images. An algorithm for calculating this optical flow has been developed. [2,3]

If $E(x,y,t)$ are the brightness values at the point x,y for an image at time t, and $u(x,y)$ and $v(x,y)$ are the horizontal and vertical components of the velocity, the velocity components can be found by satisfying the equation which tracks points of constant brightness:

$$E(x + u\,\delta t, y + v\,\delta t, t + \delta t) = E(x,y,t) \qquad (1)$$

for small changes in time. Equation 1 is solved for velocity components, which represent how the brightness value moves between frames. Expanding Equation 1 in a Taylor series, dividing by δt and taking the limit as δt approaches 0, the optical constraint equation becomes:

Since completing this research in his senior year, Ben has graduated from Loyola College with an interdisciplinary degree in Biology and Physics. He is currently enrolled at Embry-Riddle Aeronautical University at Daytona Beach performing graduate work in Aerospace Engineering as well as teaching Electrical Engineering Lab. When not busy with school work, Ben spends his time designing computer games and piloting airplanes.

Ryan is a first year graduate student studying astrophysics at the Johns Hopkins University. This research was begun during the summer after his junior year through a Hauber Research Fellowship and was continued during his senior year under the guidance of Dr. Mary Lowe with the support of an NSF award. Ryan also enjoys singing with an amateur band in the Baltimore-Washington area.

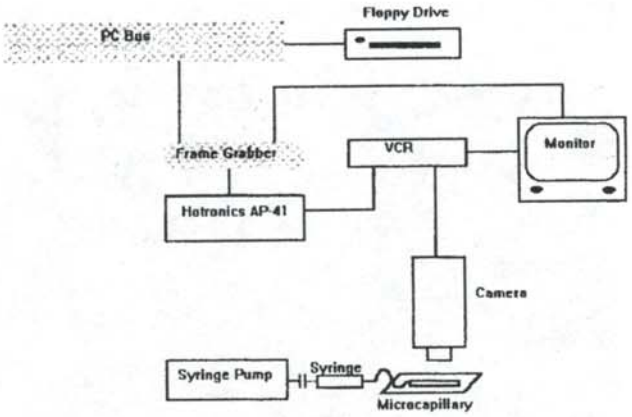

Figure 1
Hardware diagram for generating, recording and digitizing particulate flows.

$$u\frac{\delta E}{\delta x} + v\frac{\delta E}{\delta y} + \frac{\delta E}{\delta t} = 0 \ . \qquad (2)$$

The optical flow method requires a brightness gradient to compute the motion of a brightness field. It cannot calculate the component of the velocity tangent to an isobrightness contour.

The method of finding the velocity components is accomplished by using the calculus of variations. Because the images are captured as an array of discrete pixels, the problem must be solved for the discrete case. The result is an iterative scheme. If i and j are the pixel coordinates and n is the value of the iteration:

$$u_{ij}^{n+1} = \overline{u_{ij}^{n}} - \beta\frac{\delta E}{\delta x}$$
$$v_{ij}^{n+1} = \overline{v_{ij}^{n}} - \beta\frac{\delta E}{\delta y}\,, \qquad (3)$$

where

$$\beta = \frac{\overline{u_{ij}^{n}}\frac{\delta E}{\delta x} + \overline{v_{ij}^{n}}\frac{\delta E}{\delta y} + \frac{\delta E}{\delta t}}{1 + \lambda\left[\left(\frac{\delta E}{\delta x}\right)^2 + \left(\frac{\delta E}{\delta y}\right)^2\right]}\,, \qquad (4)$$

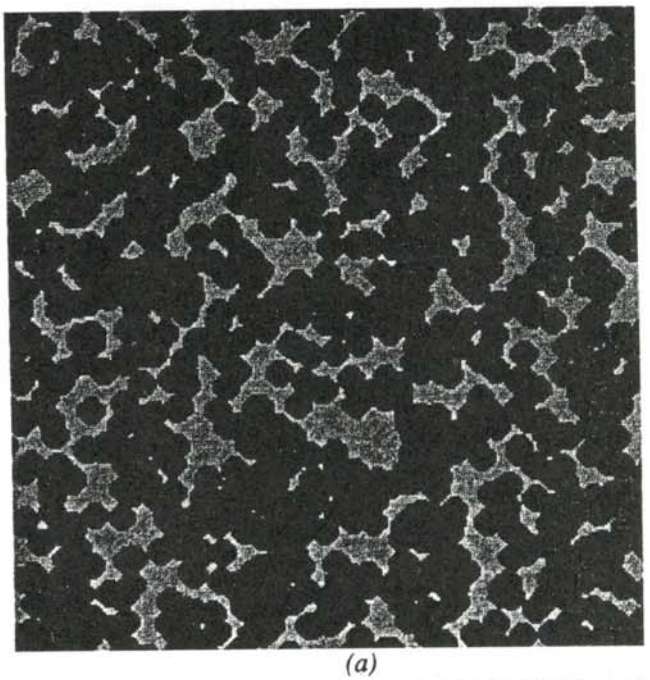

(a)

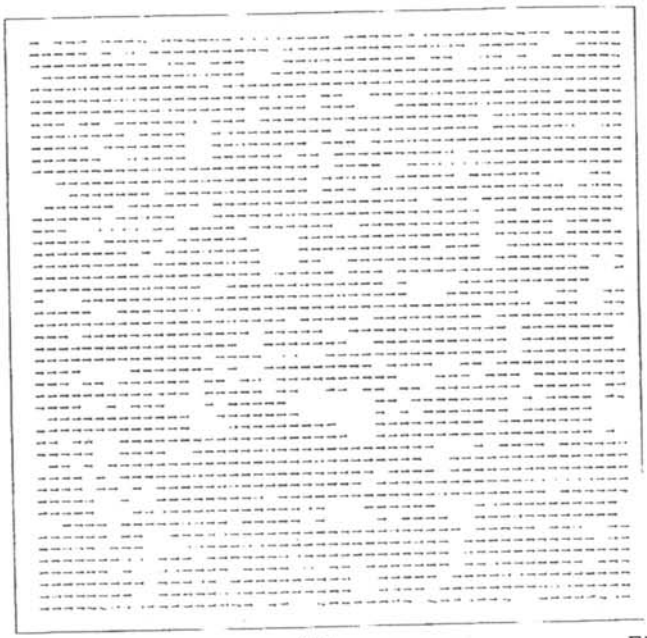

(b)

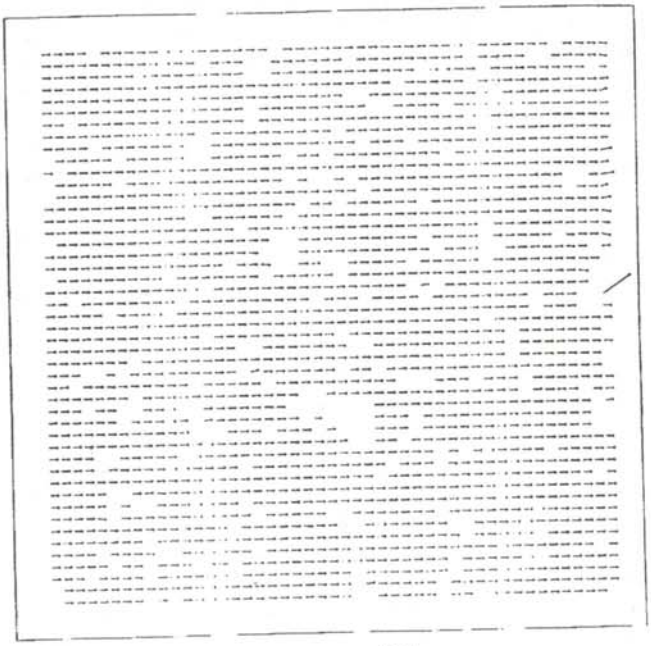

(c)

Figure 2
a) Single frame of simulation particles moving at 1 pixel/frame. b) Motion field of two successive frames using the Horn Method. c) Motion field corresponding to nine successive frames using the multi-frame Horn method.

where $\overline{u}_{ij}^{n}$ and $\overline{v}_{ij}^{n}$ are the local averages of u and v. The quantity λ is a parameter that weights the error in the image motion relative to the departure from smoothness.

Equations 3 are developed for two images. Another approximation can be obtained by using several images weighted by a Gaussian distribution about a central image. The number of images required is defined by the standard deviation of the Gaussian. The Horn and Schunck algorithms were obtained from an anonymous FTP site (chaplin@csd.uwo.ca). We executed the codes on a Silicon Graphics IRIS Indigo Workstation with a R4000/ 100 MHz CPU.

METHODS

To generate experimental data for optical flow analysis, we constructed a capillary flow similar to that in blood vessels. We used a .25 microliter Cole Parmer micropipet with an outer diameter of .020" and an inner diameter of .0039". This was inserted about 1 cm deep into .020" ID teflon tubing. To insure no leakage, the entire junction was coated with a fast drying epoxy. The micropipet assembly was then taped to a microscope slide and mounted under a Nikon Labophot-2 upright microscope.

Using a B-D 3 cc syringe with a 1% solution of 5.2 micron polystyrene beads, we filled the teflon tubing and micropipet. A Hamilton 710RN 25 microliter syringe, filled with distilled water, was then mounted on a Harvard Apparatus 33 syringe pump and inserted into the other end of the teflon tubing. The pump was then operated at .4 microliters per minute to procure a steady flow.

The particulate flow was viewed using normal light microscopy under a 40X objective and with an extremely small lamp aperture setting which enabled a greater depth of field, making more particles above and below the focal plane detectable. The flow was recorded on a SVHS tape using a Pulnix TM-545 black and white CCD camera and an All-tronics VCR. The images were digitized frame-by-frame using an IBM PS/2 equipped with a Data Translations DT2953 frame grabber card and Qcapture version 5.3 software. The frames were saved to disk and transferred to the Silicon Graphics workstation. Optical flow algorithms were then executed to produce the motion field.

RESULTS

To obtain a flow with know velocities, we generated a series of 300 by 300 images which simulated particles moving from left to right at a constant rate of 1 pixel per frame as shown in Figure 2a. The two-frame optical flow method yielded the motion field shown in Figure 2b. Using nine consecutive frames and the multiple frame Horn method with a standard deviation of 0.75, we produced the motion field shown in Figure 2c. For this simulated data and the subsequent experimental data, we ran optical flow algorithms for 100 iterations and with $\lambda = 0.5$.

For the simulated data, the calculated mean velocity was 1.000±.002 pixels/frame. When there were no particles in the image, Figure 2a, and thus constant brightness, no

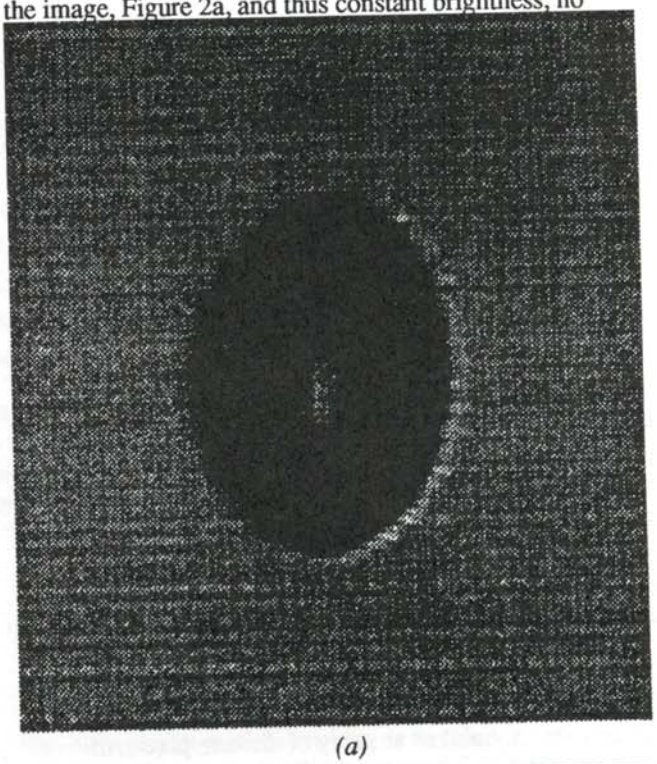

(a)

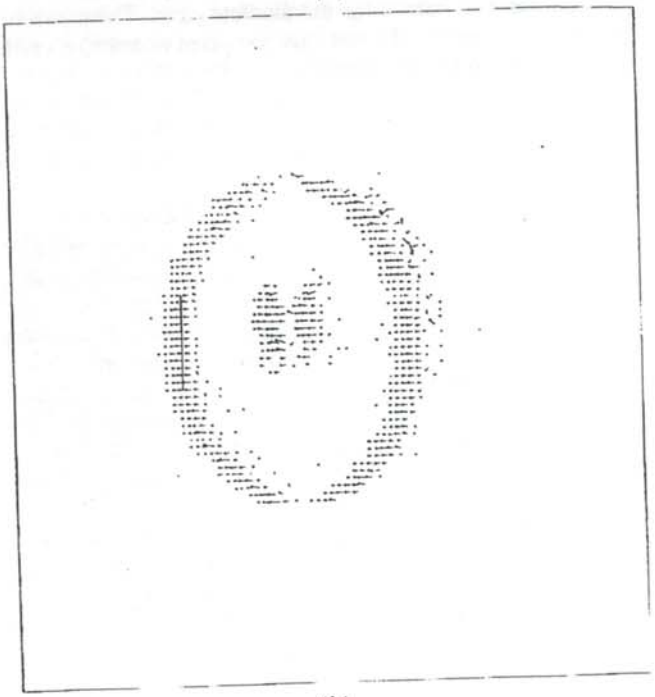

(b)

Figure 3

a) single frame of a bubble moving to the left. b) Motion field resulting from the two-frame Horn method with velocity thresholding. Manual and computed velocities along the line are 5.0±0.5 and 4.5±0.3 pixels/frame respectively.

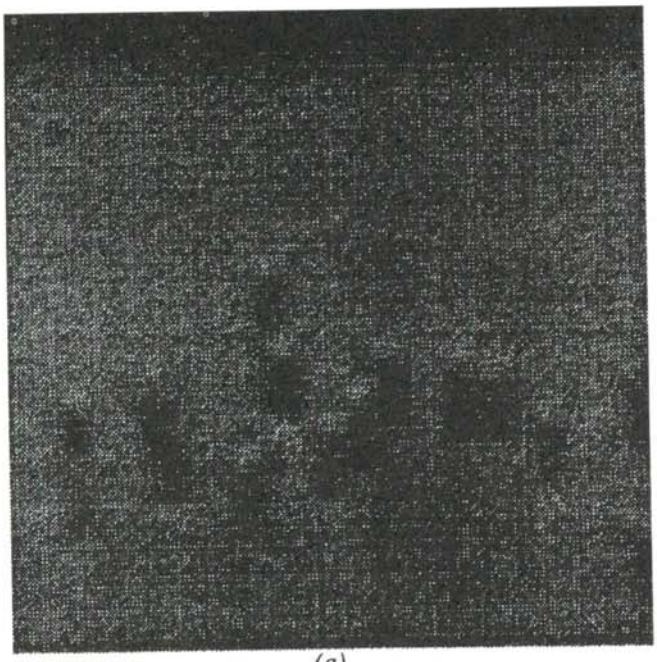

(a)

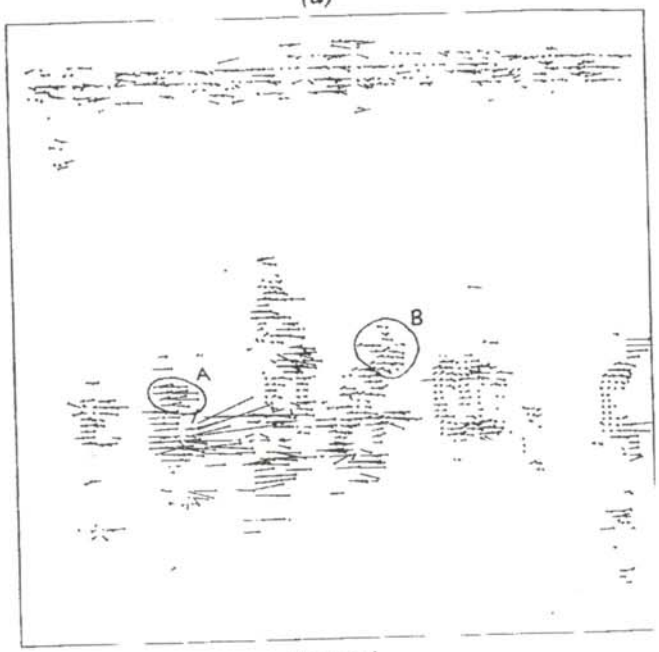

Figure 4

a) single frame of a multi-particle flow. b) Motion field resulting from the two-frame Horn method with velocity thresholding. Regions A and B are two sets of vectors associated with two different particles.

velocity vectors can be computed, causing gaps in the motion field, Figures 2b and 2c. The optical flow method is not valid at the edges of the image, as shown by the deviation of the vectors from the actual horizontal motion. This problem is even more pronounced in the multi-frame method where the particles disappear from the field-of-view in later frames, see the right edge of Figure 2c. In both motion fields, vectors also deviate near particle edges that are parallel to the direction of the flow. This effect is again greater in the multi-frame method, Figure 2c, because of the larger distances that the parallel edge travels over the series of frames.

Moving Bubble

To test the optical flow algorithms on actual experimental data, a videotape of a deforming single bubble moving from left to right was obtained as shown in Figure 3a. A manual estimate of the velocity of the left edge of the bubble was 5.0±0.5 pixels/frame. Using the two-frame Horn method, we generated the motion field of the bubble, shown in Figure 3b. The calculated average velocity of the left edge for points along the line perpendicular to the flow was 4.5±0.3 pixels/frame. The extremely small vectors on either side of the line are mostly due to the intensity gradient in each frame, not the motion of the bubble.

The absence of vectors inside the constant dark region of the bubble results from a nonexistent gradient. The deficiency of vectors at the top and bottom of the bubble is due to the problem of finding velocities of an edge parallel to the direction of motion. The vectors in Figure 3b that deviate drastically from the expected horizontal motion are the effects of an indistinct gradient in that region. Despite these few idiosyncrasies, optical flow algorithms provide an excellent qualitative velocity map. With proper interpretation, they provide accurate quantitative information.

Multiparticle image

Figure 4a shows one image of a multiparticle flow using the experimental method outlined earlier. The time between two successive frames was 0.2 seconds. A calculation shows that each pixel corresponds to 0.400±.006 microns. The velocity of any particular particle varies with its location in the capillary. Figure 4b is the motion field calculated using the two-frame Horn method. The motion field indicates that some particles are moving faster than others. For example, the average velocity of the particle in region A of Figure 4b was 3.0±.3 pixels/frame. For region B, the average velocity was 1.3±.3 pixels/frame. The average velocity magnitude for all the particles was 2.5±.5 pixels/frame or 5.0±.1 microns/second.

The random vectors at the top of Figure 4b occur at the edge of the capillary where there were small random fluctuations in the intensity gradient. Since there was no net movement of the capillary wall, these small fluctuations gave rise to the random vectors, especially in the horizontal direction where the gradient is not distinct. The stronger gradient in the vertical direction limits this effect for vertical vector components. The effects of noise upon the performance of the optical flow algorithms are not well understood.

SUMMARY

Optical flow algorithms are useful for calculating two-

dimensional velocity fields. The apparent motion in the brightness field corresponds to the motion field.

Optical flow algorithms require a distinct intensity gradient. The method fails if the object is near the boundary of the image or if an edge moves past this boundary. The velocity component of an edge parallel to the flow cannot be computed reliably. Therefore, not every velocity vector associated with a moving particle is a valid measurement of the actual velocity. Interpretation is required to obtain accurate quantitative information, but the qualitative features produced by the optical flow algorithms are very helpful in analyzing fluid flows.

ACKNOWLEDGMENTS

The authors would like to thank Dr. Roger Eastman for introducing us to optical flow, Dr. Darren Hitt for his aid with the computer analysis and simulated data, and Dr. Ali Kolaini for the bubble data. This work was supported by the Physics Department at Loyola College, the Hauber Research Fellowship of Loyola and NSF PFF Award CTS-9253633.

REFERENCES

* Present address of author: Department of Physics and Astronomy, Johns Hopkins University, 3400 N. Charles Street, Baltimore, MD 21218.
** Present address of author: Embry-Riddle Aeronautical University, Department of Aerospace Engineering, 600 South Clyde Morris Boulevard, Daytona Beach, FL 32114-3900

1. For a review see Paul C. Johnson, "Flow Measurement in the Microcirculation", Charles H. Baker and William L. Nastuk, editors, Microcirculatory Technology, Academic Press, Orlando, Florida, (1986).
2. Berthold Klaus Paul Horn, Robot Vision, The MIT Press, Cambridge, Massachusetts, (1986).
3. B.K.P. Horn and B.G. Schunck, "Determining Optical Flow", Artificial Intelligence, 17, (1981), p. 185.

FACULTY SPONSOR

Dr. Mary Lowe
Physics Department
Loyola College
Baltimore, MD 21210

POLYELECTROLYTE GELS AS ARTIFICIAL MUSCLE SYSTEMS

Kimberly Branshaw, Dana Deardorff and Garrett Davis
Laboratory for Materials Physics
Illinois Wesleyan University
Bloomington, IL 61702-2900
received June 28, 1994

ABSTRACT

Electromotility, the bending in response to an electric field, of polyelectrolyte gels in ionic solutions has been identified as a candidate for a potential chemomechanical engines such as muscles. We discovered that the underlying physics of these systems is more complex than previously believed. We found that the bending as a function of time obeys a square root power law. This points strongly towards a diffusion mechanism for the bending. Kinetic evidence for diffusion was independently corroborated by experiments on gels grown or bent in the presence of dyes. We explored the effects of varying poly-ion concentration in the backbone of the polymer and in the surrounding medium. In some cases, the electromotility cannot be described as simple bending.

INTRODUCTION

Traditionally, it requires two steps to convert chemical energy into mechanical energy. First, a battery or power plant converts chemical energy into electric energy, which in turn drives a motor to produce kinetic energy. There is significant interest in integrating these two steps into one and making a "chemomechanical engine". A naturally occurring chemomechanical engine is muscle tissue. During the past nine years, polyelectrolyte gels in ionic solutions have been investigated as artificial muscle-like materials. [1,2,3] These gels undergo large reversible bending motions in response to an applied electric field.

Kimberly is a senior with a double major in physics and chemistry. She has won the best undergraduate research presentation award at two consecutive annual meetings ('94 and '95) of zone 9 of the Society of Physics students. She will attend graduate school in materials science, probably at Northwestern University.
Dana is a senior physics major. This research, which was presented at two national conferences, resulted in a strong interest in biomechanics and other areas of physics in biomedicine. He is planning to attend graduate school in biomedical engineering at UC-Berkeley.
Garrett received his bachelor's degree from IWU in 1994 and is enrolled in the 3-2 dual degree program. He will receive a B.S. in electrical engineering this summer from Washington University and will probably go on to graduate school.

A gel is a state of matter that is intermediate between a liquid and a solid. Gels have properties of both of these states of matter. They support a shear stress like solids, but still allow mass and charge diffusion like liquids. A polymer is a chain of basic chemical units, called monomers, that are covalently linked together in a solvent. In the solvent, the polymer chains behave like a highly viscous liquid. If the polymerization process occurs in the presence of a cross linking agent, two monomer units joined by a side chain, permanent links would be formed at random positions between the long polymer chains in the solvent. This creates a complex network of branches and interconnections.[4] At this point, if the solvent were allowed to evaporate from the polymer, a hard solid would result.

If these polymers are allowed to become swollen with a solvent, they become gels. The solvent is held inside the gel by a hydrophilic network of these long cross linked chains. [4] The gels have solid-like properties due to the geometrical constraints enforced by the cross linked network of polymer, yet display liquid-like properties due to the free flowing solvent within the solid-like structure. The structure of the gel is maintained by the electrostatic repulsions of the side linking chains and the osmotic pressure caused by the ions in the solvent. [4]

THE EXPERIMENT

Preparation of the gels

The gels were prepared in the following way. Acrylic acid, acrylamide, sodium hydroxide and

N,N-methylenebisacrylamide were dissolved in water with mole ratios of 0.1, 0.1, 0.1 and 0.001 respectively to make a total volume of 50 ml. 50 mg of potassium persulfate and 0.2 ml of N,N,N'N'-tetramethylethlyenediamine (TEMD) were added to this mixture to polymerize the gels.[5] The gelation time was dependent on the concentration of the potassium persulfate and TEMD, the temperature of the solution and the volume of the gel made. In our case, the gelation time ranged between 5 and 15 minutes and the solution temperature was approximately 60 C.

For electromotility measurements, these gels were cast in 1.5 mm glass capillary tubes and removed either by pumping water through them with a syringe or shattering the capillary tube. The polymerized specimens are then swollen in deionized water for a few hours to acquire their equilibrium volume. After swelling, the rods are approximately 6 mm in diameter. They can be cut with a sharp razor blade to produce specimens of desired lengths. They tend to be a bit brittle and the cut edges are not smooth.

Electromotility Measurements

The gels are put into a conductive aqueous solvent, usually water and then placed between two parallel carbon electrodes. A DC voltage between 5 V and 50 V was applied across the electrodes which induced a current less than 150 mA through the gel. The gels have a refractive index very close to that of water. They are barely visible when submerged. Video macroscopy and computerized image processing were used to delineate the contours of the rod shaped specimens. We measured the bending (deflection) produced by the electric field as a function of time. Figure 1 shows the two enhanced video images of the apparatus. The top electrode is the anode.

The measurements were done with gels of the same diameter, but a range of lengths. We also tried different concentrations of the conductive aqueous solvent, from deionized water to 0.1 M NaCl and changed the initial shape by cutting the original gel.

RESULTS

When the voltage was applied to the apparatus, the gel began to bend towards the anode. When the polarity was switched, the gel came back to a straight shape and began to bend towards the bottom electrode. Figure 2 shows a gel that has been subjected to an electric field for approximately 5 minutes. The polarity of the field was then switched. Each successive frame had this new polarity. The time interval between each frame is 90 seconds. The total time it takes for a gel to flex from one direction to the other was between 10 to 15 minutes. This confirms that the bending depends upon the direction of the applied electric field. [1,2,3] These pictures demonstrate both the promise and the problem of using these gels as artificial muscles. To be usable in engineering applications, the bending time must be decreased to a few fractions of a second.

Figure 1
Two video images showing the electric field induced bending of the gels. The anode is the upper electrode. The two frames show different stages of video enhancement.

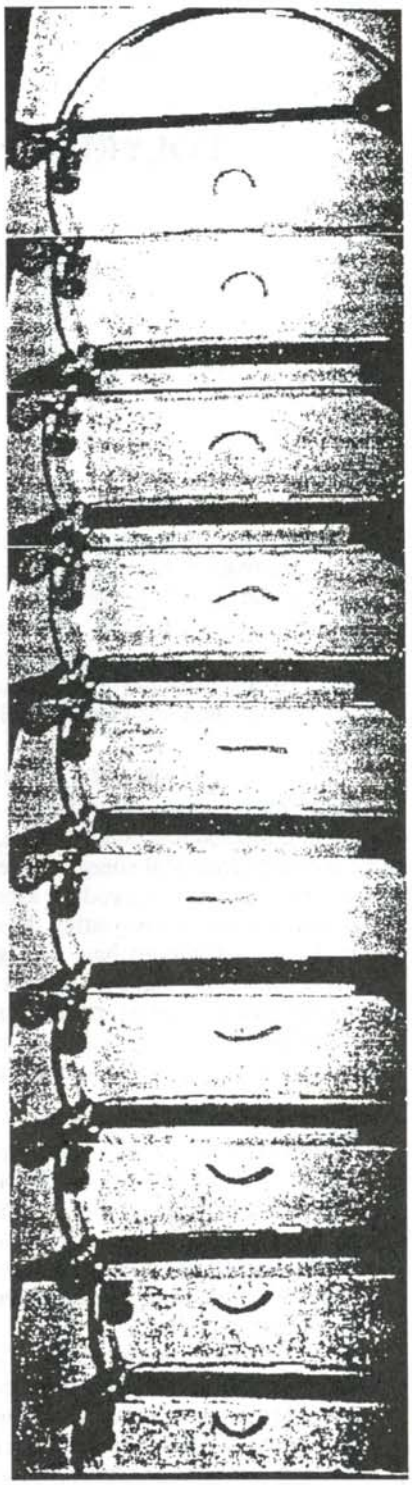

Figure 2
Flexing of a gel by reversing the direction of the electric field. there is about 90 sec time interval between each successive frame. The total time required for one bending sequence is approximately 15 min.

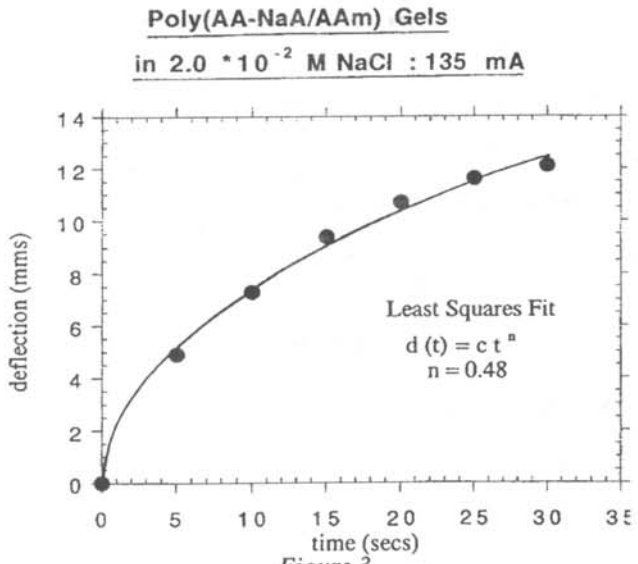

Figure 3

Results of a typical electromotility experiment. Bending is plotted as a function of time. The curve shown is a least squares fit to a simple power law function.

When the electric field is reversed, some gels show a rather complex bending behavior. On occasion, as the curvature of the gel is decreasing, the gel rod would roll about an axis parallel to its long edge. The bending always stayed consistent with the direction of the applied electric field, but the gel avoided the intermediate stages of straightening out. Other gels, go through an intermediate "S" shape before beginning to curve in the opposite direction. We will continue to examine this interesting behavior.

Figure 3 is a typical plot of the bending, d, as a function of time, t. The line drawn was a least squares fit to the data with a simple power law:

$$d(t) = c\, t^n \,. \qquad (1)$$

The different samples produced an exponent n between 0.48 and 0.55. These exponents were close enough to 0.50 for us to suggest that the bending was dependent upon the square root of the time. This dependence is strongly suggestive of a diffusional mechanism for the bending. It has been suggested that the bending results from diffusion of water into one side of the gel. That side of the gel then begins to expand more than the other side and bends to accommodate the differential swelling. The direction of the electric field determines into which side of the gel the water diffuses. The result is similar to that of a heated bimetal strip.

To directly demonstrate the diffusion process, dyes were introduced into the gel in two different ways. The dye was either dissolved in the water used to swell the polymerized and cross linked material or it was introduced into the monomer solutions used as precursors. When the swelled dyed gels were placed in undyed water, passive diffusion of the dye out of the gel occurred over a period of a few days. This showed that any passive diffusion of the dye during the few minutes that it takes for the electromotility measurements was not important.

The charge neutrality of the dyes was tested by placing them in the solvent and applying an electric field. No electrophoresis was noticed. This indicated that the dyes are charge neutral, but does not rule out the possibility that the dye molecules interact with the charge back bone of the polymer and acquire a charge when incorporated in the

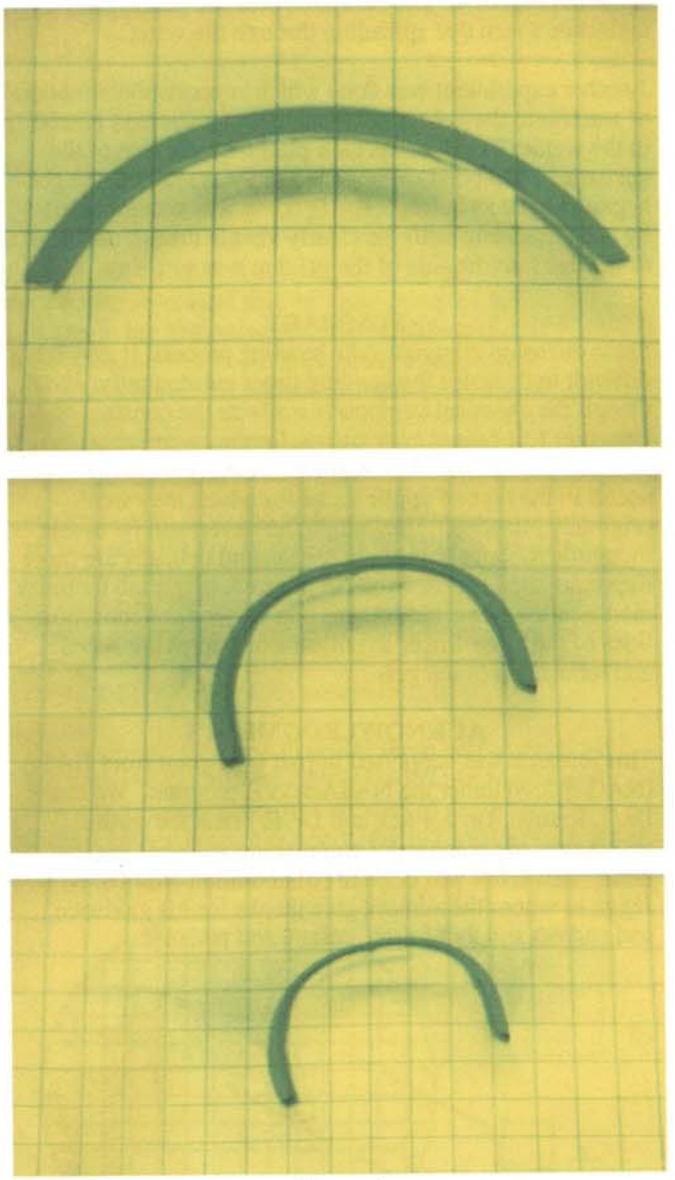

Figure 4

Direct observation of a diffusinal mechanism for the bending action. The gel was grown in the presence of malachite green dye. The dark areas near the gels are the dye diffusing out of the gel and into the clear surrounding water.

gel. We used two dyes: safranine O and malachite green. The bending kinetics of the dyed gels were found to have the same square root dependence on time as the undyed gels.

While the electromotility experiment is in progress, the dye begins to diffuse out of the gel and into the surrounding water in a matter of minutes as the bending occurs. The gel then began to appear as one part containing the dye and the other part that was clear. The diffusion of the dye into the surrounding solvent provided direct evidence of the diffusional process. Examples of this diffusion are shown in Figure 4. The dark area near the gels is the malachite green dye spreading through the water.

Another experiment was done which supports the diffusion of water into the gel. A gel containing no dye was placed in the water. The dye was then placed on the side of the gel expected to bend. When the field was applied, the gel began to bend as before. The bending was accompanied by and coincident with the clearly visible inward diffusion of the dye into the side of the gel that was swelling.

SUMMARY

Since diffusion dominates the bending process, it may be difficult to decrease the bending times substantially. Even though the chemical composition affects the constant in Equation 1, it cannot compensate for the square root dependence on time. Consequently, these gels may not be useful in the type of applications for which they were originally intended. They might, however, still be usable in 'gentle robotics', where precision and delicacy are more important than speed. Work in progress in our lab includes modification of the side chains and varying the concentrations of the cross-linker as a means of improving speed and robustness of the gels.

ACKNOWLEDGMENTS

This research was supported in part by a grant from NASA (NAG-8-258) under the NASA/JOVE program. We thank Dr. T. Rettich, Dr. J. Frick and Dr. F. Frank for careful readings of the manuscript and making valuable suggestions. This work was done in collaboration with Dr. N. K. Jaggi, to whom the authors give thanks for his guidance and endless supply of time, energy and patience.

REFERENCES

1. M. Doi, M. Matsumoto and Y. Hirose, Macromolecules, 25, (1992), pp. 5504-5511.
2. Y. Osada, H. Okuzaki and H. Hor, Nature, 355, (1992), pp 242 - 244.
3. H. Okuzaki and Y. Osada, Journal of Intelligent Materials Systems and Structures, 4, (1993), pp 50-53.
4. T. Tanaka, Scientific American, Jan, (1981), p. 127.
5. T. Shiga, T. Kurauchi, Journal of Applied Polymer Science, 39, (1990), pp. 2305-2306.

FACULTY SPONSOR

Dr. N.K. Jaggi
Laboratory for Materials Physics
Illinois Wesleyan University
Bloomington, IL 61702-2900

ART IN PHYSICS: EXOTIC MACROSTRUCTURES IN SWELLING POLYELECTROLYTE GELS

Dana Deardorff and Kimberly Branshaw
Department of Physics
Laboratory for Materials Research
Illinois Wesleyan University
Bloomington, IL 71702

received July 10, 1994

ABSTRACT

We have recently discovered, somewhat accidentally, a rare and elegant coarsening mode in the swelling of some polyelectrolyte gels that leads to intermediate structures that are quite complex and beautiful. These gels evolve from simple cylindrical shapes in the beginning to form periodic patterns of "cusps" around the edges and roughening of the surface at short times. At intermediate stages, the elegant, three-dimensional structures formed resemble a sensuous orchid. Finally, the gel returns to its original geometry as a scaled-up replica of the initial structure. Curiously, the intermediate structures, however complex, are quite reproducible in all essential features. The results and our qualitative understanding of this phenomenon are presented.

INTRODUCTION

There has been considerable interest in the past few years in the electromotility (the phenomenon of bending in response to an electric field) of polyelectrolyte gels, [1,2] Polyelectrolyte gels are a class of cross linked polymers[1] that swell considerably when placed in a solvent, up to 60 times their initial volume.

To understand the swelling process, consider the gel cylinder to be divided into a grid of smaller sections, shown in Figure 1. Each section represents a part of the gel to be swelled with water. The concentration of water into the gel has a diffusional profile and decreases as one moves inward from the periphery of the gel. Thus, a section near the center will not swell much, while a section near the periphery will swell considerably. Because all the sections near the periphery want to swell substantially, there is not sufficient space for them to grow uniformly. The geometrical space constraint of the gel itself forces the edges to "buckle" as they continue to swell.

Research is in progress to utilize these gels as artificial muscles. [2,3] Because of their intended use as artificial muscles, prior research was conducted using tiny rod-shaped gels. Through experimentation with a much larger cylindrical piece, we discovered an unusual and interesting

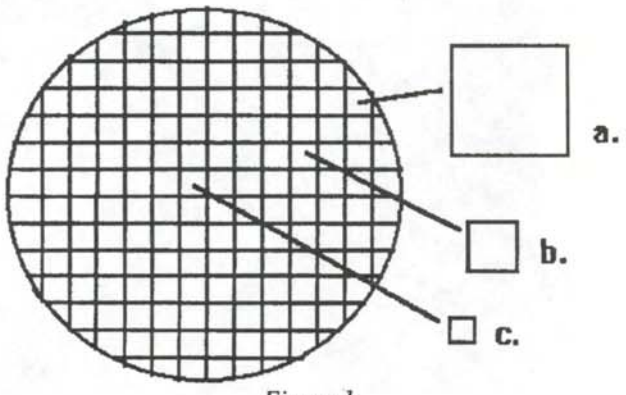

Figure 1
Schematic drawing of gel cylinder illustrating the swelling of different sections.

Dana is a senior physics major with a strong parallel interest in art. This work was stimulated by this eclectic interests in art and physics and has been presented at two national conferences. He is planning to attend graduate school in Biomedical engineering at UC-Berkeley.

Kimberly is a senior with a double major in physics and chemistry. She has won the best undergraduate research presentation award at two consecutive annual meetings (94 and 95) of Zone 9 of the Society of Physics Students. She will attend graduate school in materials science, probably at Northwestern University.

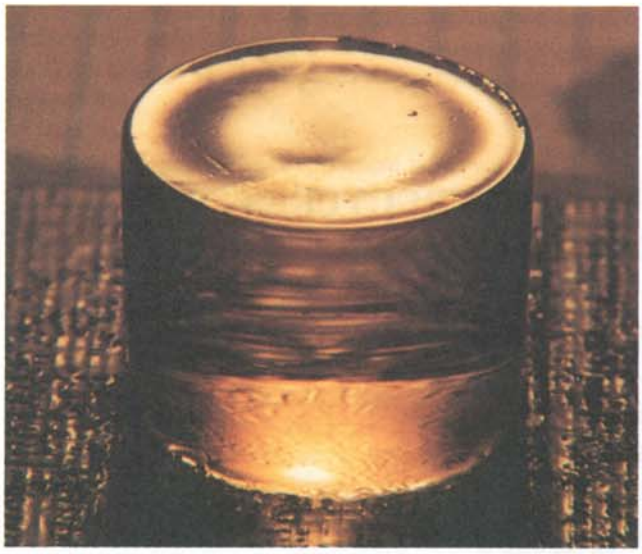

Figure 2
Photograph of the unswollen cylindrical gel. The diameter is 38 mm.

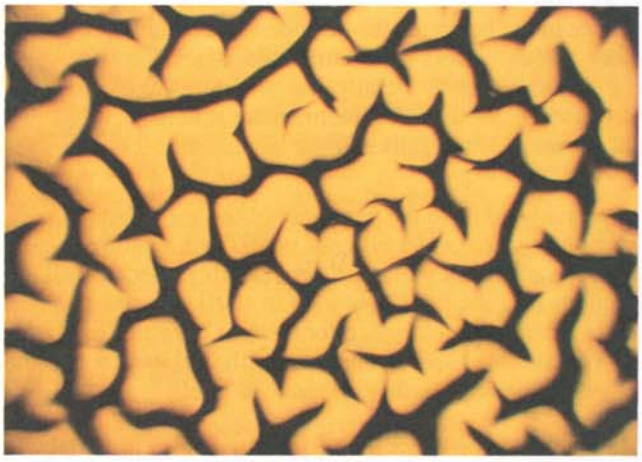

Figure 3b
Initial coarsening of the surface of the gel

Figure 4
Intermediate state of growth.

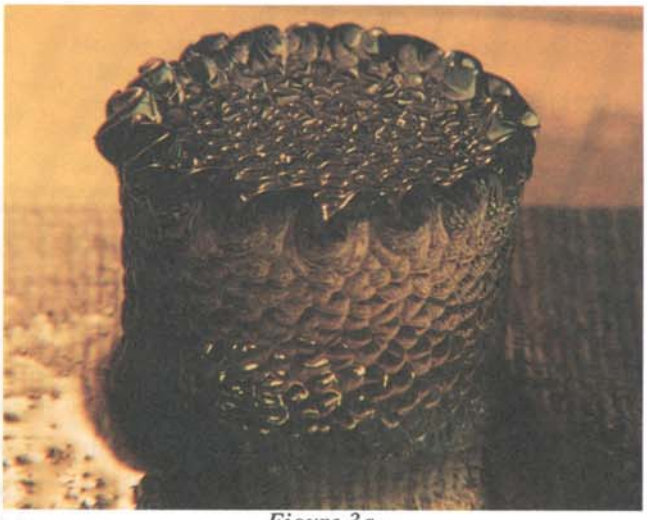

Figure 3a
Early stages of the swelling of the gel

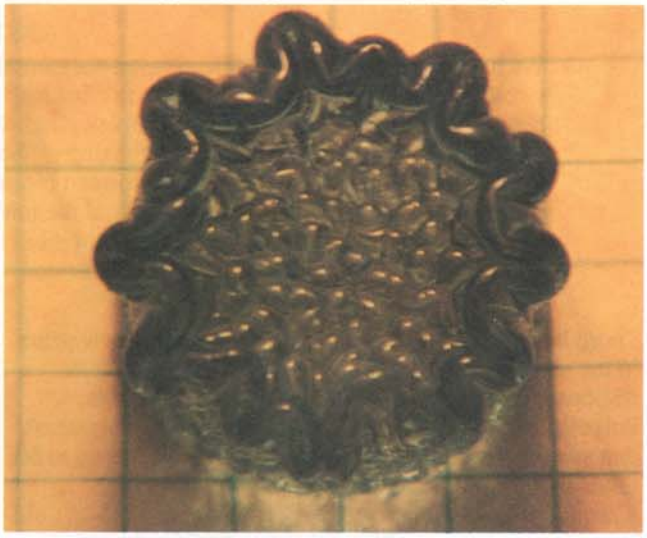

Figure 3c
"Fold pattern" at the top edge of the cylindrical gel.

Figure 5
Final stage of the growth, showing the return to original shape. The diameter is now approximately 120 mm.

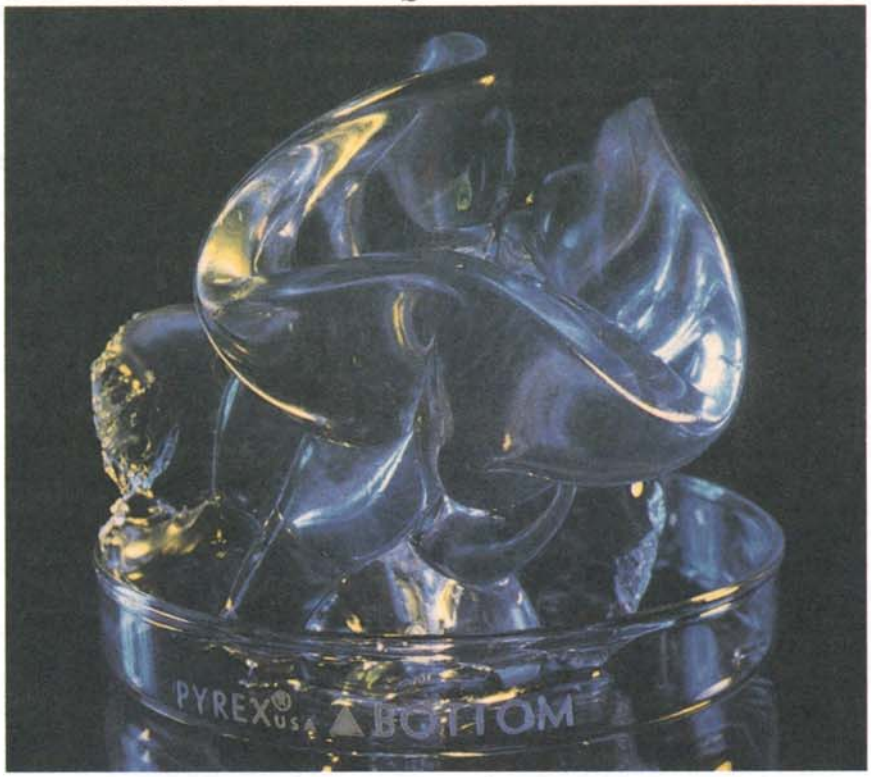

Figure 6a

Photographs of the intermediate state of a swelling gel containing a dye. The 'sculpture' in Figure 6 was illuminated with white light while the 'sculpture' in Figure 7 was illuminated with from the back with a red night lamp and a regular frosted light bulb.

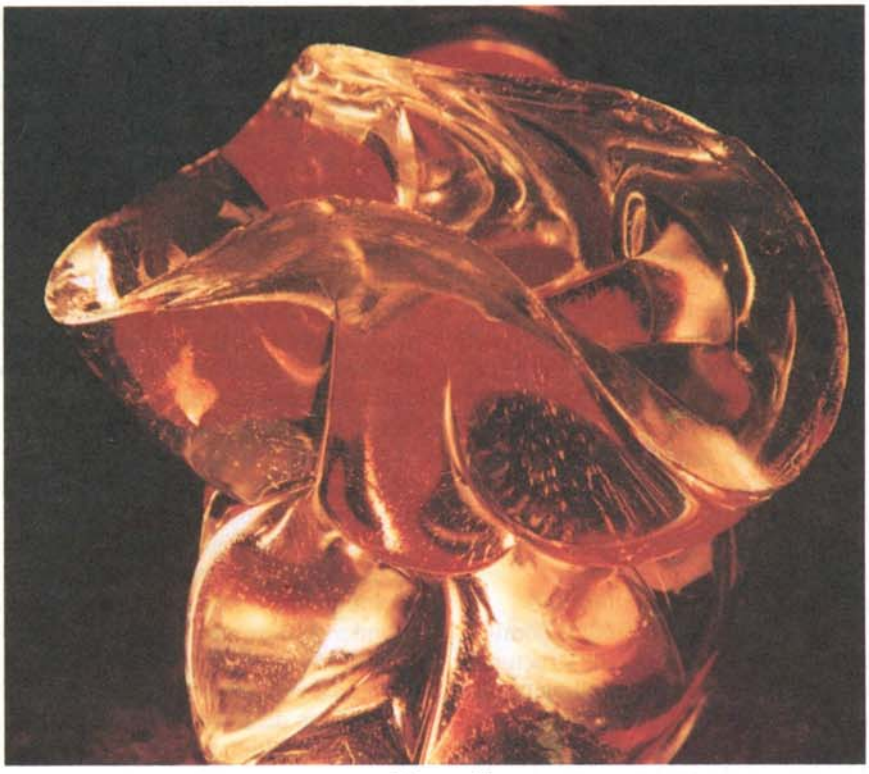

Figure 6b

phenomenon. Even though the final swollen gel has the same geometry as the starting shape of the gel, we discovered, almost accidentally, that the swelling is quite inhomogeneous during the intermediate stages. These gels undergo structural swelling transitions that are rare and quite elegant. The resulting structural forms of the gels are interestingly complex.

THE EXPERIMENT

Experiments were conducted using the cross linked Poly (AA-NaA/AAm) polyelectrolyte copolymer gel, where AA is acrylic acid, NaA is sodium acrylate, and AAm is acrylamide, with water as the swelling medium. Although other gel geometries were investigated, our research was focused primarily on right cylindrical gel pieces of varying diameter. When swollen, the gel's refractive index is nearly identical to that of water, making the gel almost invisible when submerged. Frequently so two neutral dyes, safranine-O and malachite green, were added to improve the visibility of the swollen gels. Observations and measurements were taken using still photography and video macroscopy. Complete details of the chemical composition and procedures to synthesize these gels can be found in another paper in this volume that focuses on the responses of these materials to electric fields. [3]

STRUCTURAL EVOLUTION

We have divided the swelling process into three main characteristic stages of growth. The time scale for these structural changes in not fixed, but depends upon the initial size, shape and chemical composition of the gel. The time scales indicated in parentheses in the following descriptions correspond to a typical experiment starting with a right cylindrical piece of the PAA gel with a diameter of 38 mm as shown in Figure 2.

Early Stage (several minutes).
During this initial swelling, there is not much change in the total volume. However, there is an almost immediate appearance of roughening or coarsening on all the free surfaces of the gel as seen in Figure 3a and Figure 3b. There is emergence of periodic points or "cusps" around the edges of the gel, a structure which we call the "fold Pattern" because of its apparent tendency to fold into itself during further growth evolution, see Figure 3c. The entire fold pattern is itself quasiperiodic with each repeating part being wave like. Thus, we define a wave number, k, such that $k = 2\pi/\lambda$, where λ is the dominant length scale over which the pattern repeats. The early stage is distinguished by small λ or large k.

Intermediate Stage (several hours)
During this stage, there is considerable swelling and noticeable change in the volume. The swelling is dominated by the evolution of the fold pattern as the structural form of the gel is overtaken by substantial swelling of the folds themselves as shown in Figure 4. The structural changes are now occurring on a much larger length scale (λ). As the folds at the edges of the gel are growing and increasing in size, they are also systematically reducing in number as they "dissolve" into each other. Thus, the characteristic wave number $k(t)$ is decreasing monotonically with time.

Final Stage (several days)
During this stage, the get approaches its maximum swelling potential, approximately 60 times its original volume. As the fold pattern evolves, the structure becomes much less complex. Remarkably, each get "remembers" its shape and eventually returns to that original geometric form in this much larger, swollen state. After all of these unusual structural changes, the final product is an identical, scaled up version of the original gel's geometry as shown in Figure 5.

THE AESTHETICS

Apart from the obvious scientific importance of this discovery, one is captivated by the beauty of these delicate structures. It is not often that the worlds of art and science intersect so dramatically. These materials are chemically composed of simple polymer chains and are the product of a deterministic growth process. They are not the work of an artist, but still appear to be a "work of art". Figure 6 is an example of such a work of art. They possess a magnificent aesthetic quality. Their beauty is similar to ornate crystal or glass sculptures. At one stage, they resemble an exotic and translucent orchid. As they grow, they create an ever evolving artistic forum.

RESULTS AND DISCUSSION

Qualitative Results
At first sight, these complex patterns and transitions may seem almost chaotic or random. We have discovered, however, that the structural swelling transitions, despite their apparent complexity, are essentially reproducible. In particular, the shape transformations are basically identical for similar gel geometries. Two separate gels with similar initial shapes always evolve through the same stages of transitions.

Each gel identically follows the same "path" of structural changes each time it is swollen. At any stage during the swelling process, the gel can be removed from the water and allowed to return to its original, unswollen state. If the get is then replaced in water, it evolves following the same "path" of structural transitions as before.

Quantitative Results
Because the three-dimensional structural patterns and transitions are so intricate and complicated, we initially focus attention on one simple aspect. We look at the evolution of the fold pattern at the top edge of the gel cylinder as shown in Figure 3b. We measured the total number, N, of "cusps" or folds as a function of time for three different initial gel diameters: 22 mm; 32 mm; 38 mm. These data were then fit using a least squares analysis algorithm to a power law of the form:

$$N(t) = c\, t^{n} \ . \qquad (1)$$

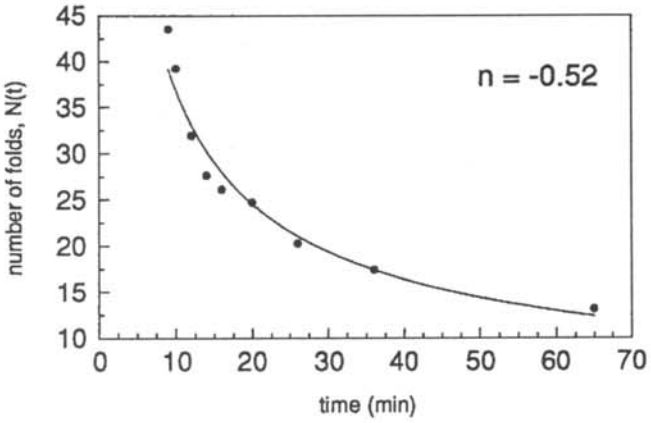

Figure 7
Evolution of fold-pattern of gel with diameter of 38 mm. The solid line is a fit to $N(t) = ct^n$.

The data and fit for one of these trials is shown in Figure 7. The three trials provided fits with exponents of n = -0.51, -0.53 and -0.52.

Since at any time, the wave number $k(t)$ is dependent upon the circumference of the cylinder of the gel itself, all trials were normalized to their initial diameter, d:

$$k = 2\,N/d \quad . \qquad (2)$$

Thus, the size differences of the initial shapes were eliminated and all data could be compared and analyzed together as a "superset" . The results for all three trials are shown together in the logarithmic graph shown in Figure 8. The power law fit from these normalized data give an exponent of n = -0.50. We find that the fold pattern evolves in time as:

$$k(t) = c\,t^{-0.5} \qquad (3)$$

Previous experimental work on pattern formation in gels was done on two dimensional surfaces, thin, flat plates tethered on one side. [6] The experimentally observed exponent in these cases was also -0.5, the same as we found in this study for three dimensional structures. After this research was completed, we became aware that the pioneering work on these gels [7] included an observation of three dimensional swelling of a spherical gel. A quantitative analysis of the three dimensional results, however, was not presented.

The functional form of Equation 3 cannot correctly represent the final stages of the swelling process. As the gel approaches its maximum swelling potential, it always returns to its original shape. The fold pattern dissolves entirely. $k(t)$ must approach 0 as time approaches infinity. Typically, a gel cylinder with a starting diameter of 38 mm will take approximately 5 days to reach its maximum swollen size. The power law cannot be expected to be applicable once the structural changes are occurring on a scale comparable to the size of the gel itself.

In previous experimental work with two dimensional cases, the inverse square root power law was found to break down for longer times, though for a different reason. Since those gels were rigidly tethered on one side, there was a permanent pattern deformation on the other free surface of the gel. Thus, $k(t)$ always approaches a finite number after long periods of time. For example, a 15 cm x 15 cm gel plate showed a constant $\lambda \approx 1.5$ cm from t = 10 hrs to more than 100 days. This strongly suggests that the equilibrium value of $k(t)$ is not zero for these tethered two dimensional gels. In our study, however, all surfaces were free and $k(t)$ eventually approached zero.

It is interesting to question whether this inverse square root dependence is valid near the beginning of the swelling. There is no reason to assume that diffusion is the dominant physical process at the earliest times.

No data were available for $k(t)$ for times less than 45 minutes. Our study of the initial swelling of the gels is shown in Figure 9. The fitted curve for this early stage of swelling gave an exponent of n = -1.07. The evolution of $k(t)$ at times less than 12 minutes was found to be more rapid than expected purely from diffusion. The surface roughening at earlier times appears to follow the more

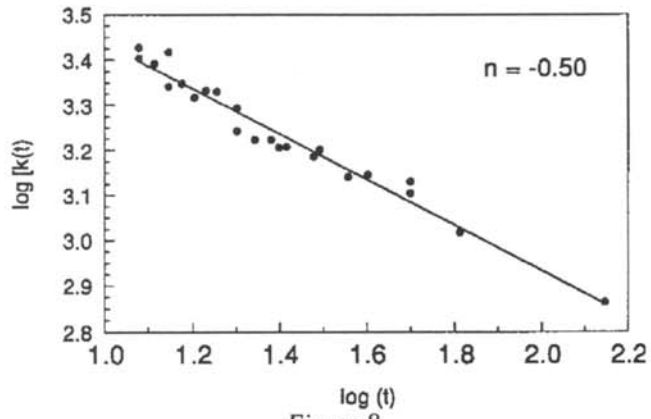

Figure 8
Evolution of fold pattern of all three gel sizes. The solid line is a straight line fit with slope = -0.50

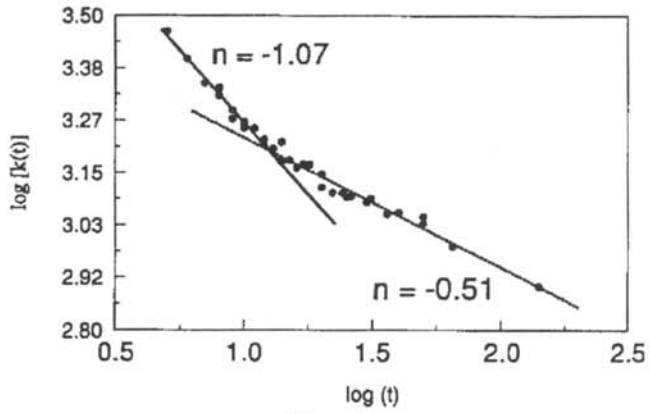

Figure 9
Evolution of fold pattern: cross over from $k(t) \alpha 1/t$ at early times to $k(t) \alpha 1/\sqrt{t}$ behavior at intermediate times.

rapid evolution

$$k(t) \alpha\ 1/t\ . \qquad (4)$$

This faster kinetic behavior is a new result.

After several minutes, the swelling follows the expected diffusional rate of Equation 3. Although the transition between these two kinds of kinetic behavior is not physically sharp, the cross over can be seen in the graph of the log[$k(t)$] vs log(t).

ACKNOWLEDGMENTS

The authors would like to express their sincere thanks to Dr. Jaggi for his gracious knowledge, guidance and encouragement at every stage of this work. This research was supported in part by a grant from NASA (NAG-8-248) under the NASA/JOVE program.

REFERENCES

1. R.S. Harland and R.K. Prud'homme, Editors, Polyelectrolyte Gels: Properties, Preparation and Applications, American Chemical Society, (1992).
2. H. Okuzaki and Y. Osada, Journal of Intelligent Material Systems and Structures, 4, (1993), p. 50
3. K. Branshaw, D. Deardorff, G. Davis, "Polyelectrolyte Gels as Artificial Muscle Systems" , Journal of Undergraduate Research in Physics, 13, 2, (1995), pp. 60 - 64.
4. A. Onuki, Phys. Rev. A., 39, (1989), p. 5932.
5. T. Hwa and M. Kardar, Phys. Rev. Lett., 61, (1988), p. 106.
6. H. Tanaka and T. Sigehuzi, Phys. Rev. E., 46, (1994), p. R39.
7. T. Tanaka, Physica, 140A, (1986), p. 261.

FACULTY SPONSOR

Dr. Narendra K. Jaggi
Laboratory for Materials Physics
Illinois Wesleyan University
Bloomington, IL 61702-2902

GAMMA RAY EMISSIONS FROM BINARY PULSAR SYSTEMS

Tony A. Hall *
Arkansas State University
Department of Physics
State University, AR 72467
received May 3, 1994

ABSTRACT

A method was developed for estimating the gamma ray flux produced in a binary pulsar system impinging upon the earth. We calculated the production of the 6.13 MeV gamma ray line produced by protons emitted by the pulsar interacting with ^{16}O atoms at the surface of the companion. We estimated the gamma ray flux at the earth as a function of proton emission from the pulsar and distance from the earth. Prospects for detection of the gamma rays on earth are discussed.

INTRODUCTION

A binary star system consists of two gravitationally bound stars, orbiting a common center of mass. A pulsar is a rapidly rotating neutron star, which , due to its intense magnetic field, emits a wide energy spectrum of charged particles and electromagnetic waves into narrow cones about each of its magnetic poles. In a binary pulsar system, one in which at least one of the stars in a pulsar, some of the protons emitted from the pulsar strike the surface of the companion star, where they interact to produce nuclear excitations. A more detailed discussion of this phenomenon can be found elsewhere. [1] Gamma rays are emitted in the de-excitation of the excited nuclei on the surface of the companion star. These gamma rays travel outward from the system and may ultimately enter a detector on the earth.

In the spectra from solar flare bursts, the most prominent gamma ray lines are the 4.43 MeV line from ^{12}C, followed by the 6.13 MeV line of ^{16}O. [2] We chose to study the production of the 6.13 MeV line since others have already focused on the 4.43 MeV line in previous solar flare work.[3]

The author graduated from Arkansas State University in May of 1994 with a B.Sc. degree in Physics. This research was begun at Goddard Space Flight Center during a summer internship. This research was presented at the first-ever Arkansas Undergraduate Research Conference on March 12, 1994 and at the meeting of the Arkansas Academy of Sciences on April 9, 1994. Tony is currently pursuing a Ph.D. degree in astrophysics at Purdue University.

THEORY AND CALCULATIONS

When a proton scatters inelastically off a target ^{16}O nucleus, the nucleus is left in an excited state and emits a gamma to reach its ground state:

$$p + {}^{16}O \rightarrow p' + {}^{16}O^*$$
$$^{16}O^* \rightarrow {}^{16}O + \gamma(6.13\,MeV) \ . \qquad (1)$$

The probability that a proton of energy E_p excite an ^{16}O nucleus located at some thickness dx a distance x from the surface of a target is given by:

$$dP(x) = \sigma(E_p)\, n_a(x)\, dx \ . \qquad (2)$$

where $\sigma(E_p)$ is the cross section for the production of the gamma ray in question and $n_a(x)$ is the number density of the target nuclei at depth x inside the target. In most laboratory experiments, $n_a(x)$ is constant and the target is so thin that the proton does not lose appreciable energy in traversing the target. In this case, an integration over the thickness of the target, t, yields the thin target approximation for the probability of interaction and of producing a gamma ray:

$$P(E_p) = \int_0^t dP(x) = \sigma(E_p)\, n_a(x)\, t \ . \qquad (3)$$

In our situation, however, the target is not thin. The protons lose energy as the penetrate into the companion star. We must employ a thick target approximation In this case, the probability of interaction in a thickness dx located at a distance x into the companion star is:

$$dP(x) = \sigma[E_p'(x)]\, n_a(x)\, dx \ , \qquad (4)$$

where E_p' is the energy of the proton after traversing the distance x into the target. We can change the variable of integration to the proton energy by:

$$dx = dE_p' \frac{dx}{dE_p'} \qquad (5)$$

where $dE_p'/dx \leq 0$ is the stopping power of the target material.

As the gamma rays are produced at increasing depths into the companion star, the probability of them escaping out of the material of the companion star decreases exponentially. As a simplification, we assume that all gammas produced within one attenuation length of the companion surface escape with a probability of 1 and all those produced further in are completely absorbed before escaping. Hence, for a proton of energy E_p entering the surface of the companion star, we allow it to lose up to the energy loss, $\Delta(E_p)$, at one attenuation length, x_γ. One attenuation length is the thickness of an absorber which will cause the gamma intensity to drop by a factor of e. The gamma ray production probability becomes:

$$P(E_p) = \int_{E_p}^{E_p + \Delta(E_p)} \sigma(E_p') \, n_a \left[\frac{dE_p'}{dx}\right]^{-1} dE_p' , \qquad (6)$$

where target density, n_α, , is the nuclear number density times a typical ^{16}O stellar abundance. The stopping power is also proportional to the nuclear number density, so our result is independent of the density of the companion star.

To find the number of gamma rays per second produced, N_γ, Equation 6, the production probability, is folded with the proton spectrum, $N_p(E_p)$ from the pulsar which strikes the companion star:

$$N_\gamma = \int_{E_t}^{\infty} N_p(E_p)\, dE_p \int_{E_p}^{E_p + \Delta(E_p)} \sigma(E_p') \, n_a \left[\frac{dE_p'}{dx}\right]^{-1} dE_p' , \quad (7)$$

where $E_t = 6.52$ MeV, the threshold energy for production of the 6.13 MeV gamma ray. The proton spectrum in Equation 7 is assumed to obey a power law and is normalized to N_p protons per second:

$$N_p(E_p) = N_p \hat{N}_p(E_p) = N_p K (E_p)^{-\alpha}, \qquad (8)$$

where the normalization constant K is determined by:

$$\int_{E_t}^{\infty} \hat{N}_p(E_p)\, dE_p = 1 . \qquad (9)$$

By inverting the order of integration and performing one integral analytically, we obtain:

$$N_\gamma = \int_{E_t}^{\infty} \sigma(E_p') \frac{n_a N_p}{(E_t)^{1-\alpha}} \left[-\frac{dE_p'}{dx}\right]^{-1} \left\{ (E_p')^{1-\alpha} - (E_p' + \Delta(E_p'))^{1-\alpha} \right\} dE_p' . \qquad (10)$$

Data for the gamma production cross section are compiled from the literature. [4] The cross section peaks in the 10-15 MeV range and falls slowly with energy as shown in Figure 1. An analytic fit to stopping power data was found in the literature. [5] The energy loss over one attenuation length is obtained from the stopping power

$$\Delta(E_p) = \int_0^{x_\gamma} \left[\frac{dE_p}{dx}\right] dx , \qquad (11)$$

where the attenuation length x_γ, was obtained by assuming a purely hydrogen composition for the companion. [6]

RESULTS

Equation 10 was integrated numerically to obtain the number of gamma rays produced per second. From supporting literature, we found that the power law constants were generally between 1.5 and 3.5. We chose the power law factor α to be 3 as an approximation to a typical power law curve. We took the proton flux, $N_p = 10^{41}$/sec to be an upper limit estimate for the Crab Pulsar based on the luminosity of the surrounding nebula. [6]

The gamma ray production per unit energy of the incoming protons, the integrand of Equation 10,

$$\frac{dN_\gamma}{dE_p} = N_p(E_p)\, P(E_p) , \qquad (12)$$

shows a peak behavior similar to the gamma ray production cross section. This is shown in Figure 2. 90% of the gamma rays are due to protons with energies Ep ≤ 50 MeV.

The gamma ray flux at the earth was found by dividing N_γ by $4\pi d^2$, where d is the distance to the pulsar. Using 1000 light-years as the distance to the nearest pulsar, we obtained:

$$\Phi_{6.13\,\gamma} = 2.4 \times 10^{-8} \frac{\gamma s}{cm^2 \sec} . \qquad (13)$$

To determine if this flux is detectable from earth, we need to consider the background signal against which it must compete. The observed energy flux from continuum

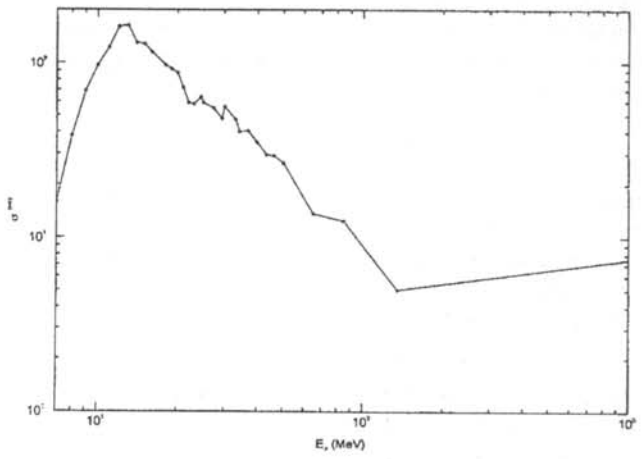

Figure 1
Cross section for production of 6.13 MeV gamma rays by scattering protons off ^{16}O.

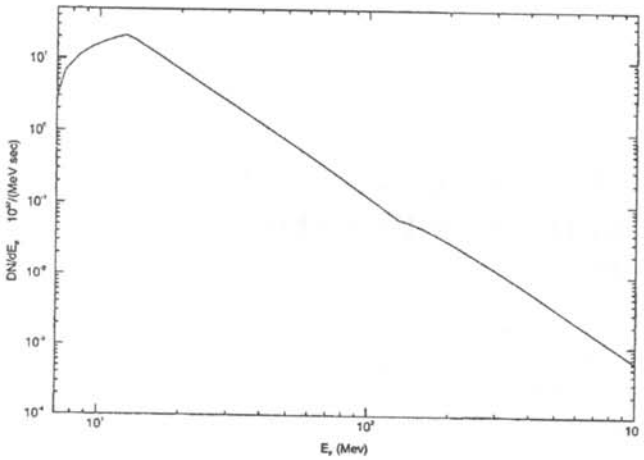

Figure 2
Production rate of 6.13 MeV gamma rays as a function of the energy of incoming protons from the pulsar.

gamma rays from the Crab Nebula is: 6

$$\frac{d\Phi_E}{dE} = 10^2 \frac{eV}{cm^2 \text{ sec } MeV}. \qquad (14)$$

At a gamma ray energy of 6.13 MeV, Equation 14 predicts a gamma ray flux of approximately

$$\frac{d\Phi_\gamma}{dE} = \frac{\Phi_E}{E_\gamma} = 1.7 \times 10^{-5} \frac{\gamma s}{cm^2 \text{ sec } MeV}. \qquad (15)$$

We take this to represent a typical background signal. The 6.13 MeV gamma ray line from ^{16}O has a full width at half maximum of about 0.1 MeV, so Equation 15 gives a background flux:

$$\Phi_\gamma = \frac{d\Phi_\gamma}{dE} 0.1\, MeV = 1.7 \times 10^{-6} \frac{\gamma s}{cm^2 \text{ sec}}. \qquad (16)$$

The flux we calculated for 6.13 MeV gamma rays from production in the surface of a companion star, Equation 13, is about two orders of magnitude smaller than the estimated background from the continuum radiation from the pulsar, Equation 16. This means that it is below detection threshold. We also calculated the gamma ray flux with $\alpha = 2$. Although it increased the flux by a factor of three, it was still an order of magnitude below detection. However, more effort should be devoted to investigating the proton flux and energy spectrum from pulsars before the detection of the gammas produced by Equation 1 can be ruled out.

ACKNOWLEDGMENTS

The author is indebted to Dr. Carl Werntz and Dr. Fred Lang for introducing him to this problem and for much useful discussion regarding its solution. The hospitality of Dr. Carol Jo Crannell and the Solar Physics Branch of NASA-Goddard Space Flight Center during visits to NASA-Goddard is gratefully acknowledged. This work has been supported by NASA-JOVE grant NAG-8-277, the Arkansas Space Grant Consortium grant NL-3013S, the Arkansas SILO Undergraduate Research Fellowship and NASA-Goddard Space Flight Center NSF-REU Program.

REFERENCES

* Present address of the author: Department of Physics, Purdue University, West Layfatte, IN 4709-1306 tahall@Bohr.physics.purdue.edu
1. M. Zeilek, S.A. Gregory and E.v.P. Smith. Introductory Astronomy and Astrophysics, Harcourt Brace Jovanovich, Orlando, (1992) pp. 328-331.
2. E.L Chupp, D.J. Forrest, P.R. Higbie, A.N. Suri, C. Tsai and P.P. Dunphy, Nature, 241, (1973), pp. 333-335.
3. C. Werntz, F.L. Lang, Y.E. Kim, Ap. J. Suppl., 73, (1990), pp. 349-357.
4. P. Dyer, D. Bodansky, A.G.Seamster, E.B. Norman and D.R. Maxon, Phys. Rev. C, 23, (1981), pp. 1865-1882. F.L. Lang, C.W. Werntz, C.J. Crannell, J.I. Tombka and C.C. Chang, Phys. Rev. C, 35, (1987), pp. 1214 - 1227. K.T. Lesko, E.B. Norman, R.M. Larimer, S. Kuhn, D.M. Meekof, S.G. Crane and H.G. Bussel, Phys. Rev. C, 37, (1988), pp. 1808 - 1817.
5. F.L. Lang, (1993), private communication.
6. M.V. Zombeck, Handbook of Space Astronomy and Astrophyhsics, Cambridge Press, New York, (1990).

FACULTY SPONSOR

Dr. Andrew Sustich
Department of Physics
Arkansas State University
State University, AR 72467-0419

THE TRANSITION BETWEEN ADIABATIC AND NONADIABATIC DYNAMIC BEHAVIOR IN A SIMPLE QUANTUM SYSTEM

Reina Maruyama *
Department of Physics and Astronomy
University of Rochester
Rochester, NY 14627
received November 15, 1994

ABSTRACT

The criterion for adiabaticity is examined for a two level atom immersed in a radiation field through a series of numerical simulations. A scheme is presented in which the degree of excitation of a two level atom can be greatly altered by changing the atom-radiation detuning parameter rapidly or slowly.

INTRODUCTION

When examining an atom that is immersed in a strong radiation field such as a laser, it is often sufficient to consider only the two energy levels of the atom that are close to the resonance with the radiation field, such that

$$E_2 - E_1 \approx \hbar\,\omega\ , \tag{1}$$

where E_1 and E_2 are the energy of the lower and upper levels respectively and ω is the angular frequency of the radiation field. Figure 1 is a sketch of such a system. The wave function, Ψ, of this "two level" atom can be written as

$$\Psi(\vec{r},t) = \sum_{n=1}^{2} c_n\,\phi_n(\vec{r})\ , \tag{2}$$

where ϕ_n is the wave function for each state. By assuming that the electron is always in either of the two states, the sum of the probabilities of the electron being in each state must add up to 1, giving

$$\left|c_1\right|^2 + \left|c_2\right|^2 = 1\ . \tag{3}$$

Schrödinger's equation for Ψ leads to first order differential equations for the two amplitudes:

$$i\hbar\frac{dc_1}{dt} = E_1c_1 + V_{12}c_2 \tag{4a}$$

$$i\hbar\frac{dc_2}{dt} = E_2c_2 + V_{21}c_1\ , \tag{4b}$$

Reina is a senior applied physics major at Columbia University. This research was done while participating in a summer research program sponsored by the NSF at the University of Rochester. She is currently applying to graduate schools to study quantum optics.

where V_{mn} is the matrix element of the interaction between the atom and the radiation field. In most cases of interest in quantum optics, this is the potential energy that comes from the interaction between the atomic dipole moment, $\boldsymbol{d}$, and the electric field of the radiation:

$$V = -\boldsymbol{d}\cdot\boldsymbol{E}(\vec{r},t)\ . \tag{5a}$$

Since we are considering only one atom, we can put it at the origin of the coordinate system, giving a potential energy

$$V = -\boldsymbol{d}\cdot\boldsymbol{E}(t)\ . \tag{5b}$$

Equations 4 can be simplified if we only consider the interaction with a quasi-monochromatic radiation field:

$$E(t) = \varepsilon_o(t)\,(e^{-i\omega t} + e^{i\omega t}) \tag{6}$$

where ω satisfies Equation 1. If $E(t)$ is sufficiently monochromatic, that is if ε_o is nearly constant with time,

$$\left|\frac{d\varepsilon_o}{dt}\right| << \omega\left|\varepsilon_o\right|\ , \tag{7a}$$

and if the anticipated resonance between the atom and the field is sufficiently sharp,

$$\left|\omega_{21} - \omega\right| << \omega\ , \tag{7b}$$

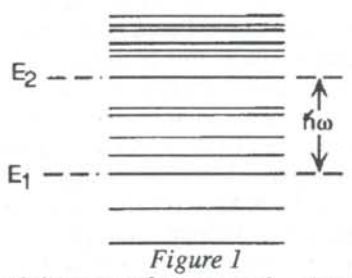

Figure 1
Energy level diagram of an atom showing the two states.

where

$$\omega_{21} = (E_2 - E_1)/\hbar \tag{8}$$

is the angular transition frequency of the atom, then the rotating wave approximation (RWA) can be used to simplify Schrödinger's equations.

We start simplifying by first defining new variables:

$$a_1 = c_1 \quad , \quad a_2 = c_2 e^{i\omega t} \ . \tag{9}$$

These new variables will satisfy the conditions

$$|a_1|^2 + |a_2|^2 = |c_1|^2 + |c_2|^2 = 1 \ . \tag{10}$$

We can substitute Equations 9 into Equations 4 to obtain equations for the a's. The RWA neglects rapidly changing exponentials and replacing factors such as $1 + e^{2i\omega t}$ or $1 + e^{-2i\omega t}$ by 1. After applying the RWA, Schrödinger's equations become:

$$i\frac{da_1}{dt} = -\frac{1}{2}\chi a_2 \tag{11a}$$

$$i\frac{da_2}{dt} = \Delta a_2 - \frac{1}{2}\chi a_1 \ , \tag{11b}$$

where

$$\Delta = \omega_{21} - \omega \tag{12a}$$

is called the detuning of the atomic transition frequency from the radiation frequency, and

$$\chi = \frac{2\, d\, \varepsilon_o}{\hbar} \tag{12b}$$

is called the Rabi frequency of the interaction, assumed here to be a real number.

By introducing the new dimensionless parameters,

$$\delta = \frac{\Delta}{\chi} \quad \text{and} \quad \tau = \chi t \ , \tag{13}$$

Schrödinger's equations become fully dimensionless:

$$i\frac{da_1}{d\tau} = -\frac{1}{2}a_2 \tag{14a}$$

$$i\frac{da_2}{d\tau} = \delta a_2 - \frac{1}{2}a_1 \ . \tag{14b}$$

In this paper, our focus will be on a comparison between solutions to the RWA equations when the parameters of the Hamiltonian are strictly constant and when they are allowed to vary slowly in time (the adiabatic case). A more detailed discussion of related questions in quantum optics of two level atoms can be found elsewhere.[1]

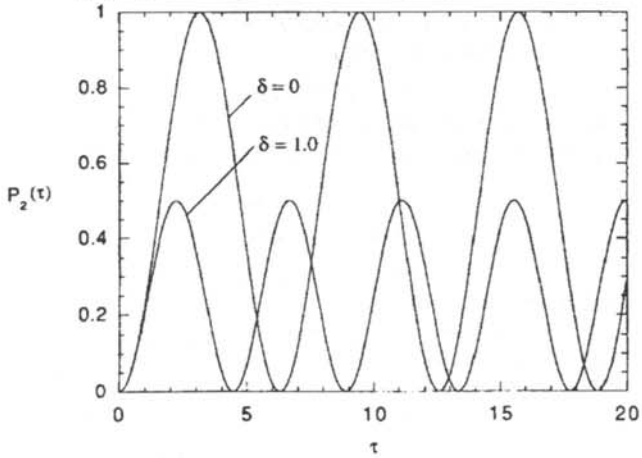

Figure 2
Rabi oscillations for different values of δ.

STEADY EXCITATION

The solutions to Equations 14 for a strictly monochromatic radiation field (constant amplitude and frequency) can be found in terms of $\Omega^2 = 1 + \delta^2$, where Ω is called the generalized or detuning-dependent Rabi frequency. For the most common case, where the atom is in the lower state initially, that is $a_1(0) = 1$ and $a_2(0) = 0$,

$$a_1(\tau) = \left[\cos\left(\frac{\Omega\tau}{2}\right) + i\,\frac{\delta}{\Omega}\,\sin\left(\frac{\Omega\tau}{2}\right)\right] e^{i\delta\tau/2} \tag{15a}$$

$$a_2(\tau) = i\left[\frac{1}{\Omega}\sin\left(\frac{\Omega\tau}{2}\right)\right] e^{i\delta\tau/2} \ . \tag{15b}$$

The probabilities undergo Rabi oscillations:

$$P_1(\tau) = |a_1|^2 = \cos^2\left(\frac{\Omega\tau}{2}\right) + \left(\frac{\delta}{\Omega}\right)^2 \sin^2\left(\frac{\Omega\tau}{2}\right) \tag{16a}$$

$$P_2(\tau) = |a_2|^2 = \left(\frac{1}{\Omega}\right)^2 \sin^2\left(\frac{\Omega\tau}{2}\right). \tag{16b}$$

The periodic nature of these solutions is shown graphically in Figure 2. Note that when δ, the normalized detuning, is constant in time, complete inversion (where a_1 becomes 0 and a_2 becomes 1) is impossible unless $\delta = 0$.

ADIABATIC EXCITATION

Schrödinger's equations (Equations 14) can be written in matrix form as:

$$i\frac{d}{d\tau}\begin{bmatrix} a_1 \\ a_2 \end{bmatrix} = \begin{bmatrix} 0 & -\frac{1}{2} \\ -\frac{1}{2} & \delta \end{bmatrix}\begin{bmatrix} a_1 \\ a_2 \end{bmatrix}, \tag{17a}$$

or

$$i\frac{d\Psi}{d\tau} = \mathrm{M}\,\Psi \ , \tag{17b}$$

where

$$\Psi = \begin{bmatrix} a_1 \\ a_2 \end{bmatrix} \quad \text{and} \quad \mathrm{M} = \begin{bmatrix} 0 & -\frac{1}{2} \\ -\frac{1}{2} & \delta \end{bmatrix}. \tag{18}$$

Since the matrix M is of second order, it has two eigenvalues and eigenvectors. The eigenvalues represent the energy in units of χ and the corresponding eigenvectors represent the wave function of each of the states. These eigenvalues are different from the energies E_1 and E_2 because they include the effect of the laser interaction and E_1 and E_2 only refer to the "bare" atomic energy levels.

Finding the eigenvalues

To obtain the eigenvalues and eigenvectors, we must solve

$$\mathrm{M}\,\Psi = \lambda\,\Psi \ , \tag{19}$$

where λ is the eigenvalue. This equation has nontrivial solutions when

$$\det(M - \lambda I) = 0 , \qquad (20)$$

where I is the identity matrix. The characteristic equation is $\lambda^2 - \delta\lambda - 1/4 = 0$ and the solutions to Equation 20 are:

$$\lambda_+ = \frac{\delta}{2} + \frac{1}{2}\sqrt{\delta^2 + 1} \qquad (21a)$$

$$\lambda_- = \frac{\delta}{2} - \frac{1}{2}\sqrt{\delta^2 + 1} . \qquad (21b)$$

Plots of these eigenvalues as a function of δ are shown in Figure 3.

Finding the eigenvectors

The eigenvectors can be found by solving Equation 19 for the normalized Ψ that satisfies Equation 10. There are two solutions for a_1 and a_2 corresponding to $\lambda = \lambda_+$ and $\lambda = \lambda_-$:

$$a_{1\pm} = \frac{1}{\sqrt{1 + 4|\lambda_\pm|^2}} \qquad (22a)$$

$$a_{2\pm} = \frac{-2\lambda}{\sqrt{1 + 4|\lambda_\pm|^2}} . \qquad (22b)$$

The eigenvectors can be written as

$$\psi_+ = \begin{bmatrix} a_{1+} \\ a_{2+} \end{bmatrix} = \frac{1}{\sqrt{1 + 4|\lambda_+|^2}} \begin{bmatrix} 1 \\ -2\lambda_+ \end{bmatrix} \qquad (23a)$$

$$\psi_- = \begin{bmatrix} a_{1-} \\ a_{2-} \end{bmatrix} = \frac{1}{\sqrt{1 + 4|\lambda_-|^2}} \begin{bmatrix} 1 \\ -2\lambda_- \end{bmatrix} . \qquad (23b)$$

It is a key to our discussion to note that the eigenvector ψ_+ coincides with the ground state if δ is very large and negative, and it coincides with the excited state if δ is very large and positive:

We can make a connection with the case discussed in the previous section, where the initial conditions are $a_1(0) = 1$ and $a_2(0) = 0$ by simply starting Ψ_+ with δ having a very large and positive value.

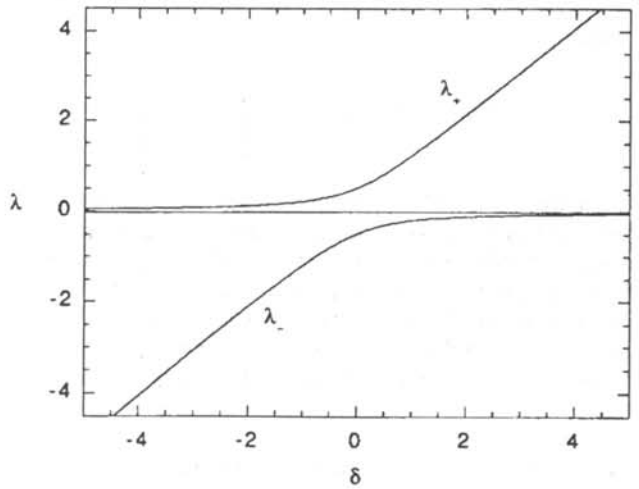

Figure 3
The two normalized eigenvalues as a function of δ.

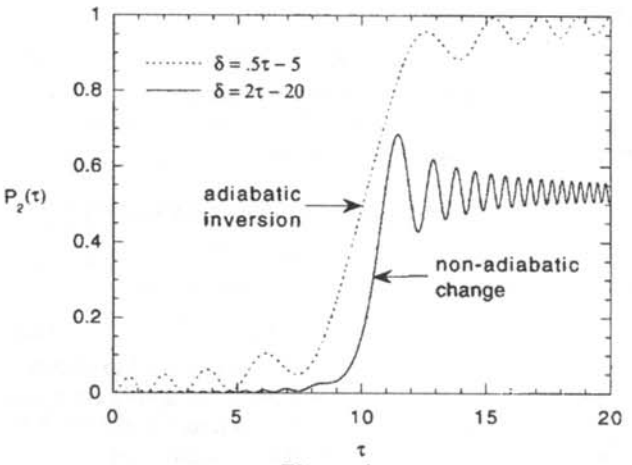

Figure 4
Adiabatic and non-adiabatic inversion processes for different $\delta(\tau)$.

$$\lim_{\delta\to-\infty} \lambda_+ = 0 , \quad \lim_{\delta\to-\infty} \psi_+ = \begin{bmatrix} 1 \\ 0 \end{bmatrix} \qquad (24a)$$

$$\lim_{\delta\to+\infty} \lambda_+ = \delta , \quad \lim_{\delta\to+\infty} \psi_+ = \begin{bmatrix} 0 \\ -1 \end{bmatrix} . \qquad (24b)$$

Equations 24 suggest that the atom can be excited with 100% probability just by sweeping δ from a very large negative value to a very large positive value. Since in this case, δ is no longer constant with time, numerical solutions are necessary to confirm this. Figure 4 shows two specific time dependences of $\delta(\tau)$ used to integrate Equations 14. The probability of the atom being in the excited state, P_2, is shown. Each curve represents a different rate of change in δ in the same time period. Of the two cases shown, one is successful in producing nearly complete inversion and one is not. This can be explained by the adiabatic principle.

THE ADIABATIC PRINCIPLE

Consider the matrix form of Schrödinger's equation (Equation 17b) again. If Ψ and M are simply numbers, the solution would take the form

$$\Psi(\tau) = e^{-iM\tau}\Psi(0) . \qquad (25)$$

However, since they are not, the eigenvalues of M must be used instead. Each component of Ψ becomes

$$a_1(\tau) = A_1 e^{-i\lambda_+\tau} + B_1 e^{-i\lambda_-\tau} \qquad (26a)$$

$$a_2(\tau) = A_2 e^{-i\lambda_+\tau} + B_2 e^{-i\lambda_-\tau} \qquad (26b)$$

where λ_+ and λ_- are given by Equations 21. This is the real solution only when the λ's are constant. If the λ's change with time as they did in the previous section, the solution is only an approximation. The approximated eigenvectors in Equations 26 will change because of both the explicit time dependence and the implicit time dependence due to the fact that $\lambda_\pm$ will change with time if δ changes with time. For the approximation to be valid, *the*

implicit change should be much slower than the explicit change. This is the adiabatic principle.

A new parameter θ, where $\sin(\theta) = 1/\Omega$ and $\cos(\theta) = \delta/\Omega$, can be introduced to compare the rates of change of the approximated eigenvectors and Equations 26. Note that $\sin^2(\theta) + \cos^2(\theta) = (1/\Omega)^2 + (\delta/\Omega)^2 = 1$ because $\Omega^2 = 1+\delta^2$. Using some trigonometric identities, one can show that:

$$\psi_+ = \begin{bmatrix} a_{1+} \\ a_{2+} \end{bmatrix} = \begin{bmatrix} \sin\left(\frac{\theta}{2}\right) \\ \cos\left(\frac{\theta}{2}\right) \end{bmatrix} . \qquad (27)$$

Changes in θ can be used as a substitute for changes in ψ_+ because any change in θ due to a change in δ will be reflected immediately as a change in ψ_+. Since

$$\frac{da_1}{d\tau} = -i\lambda_+ A_1 e^{-i\lambda_+\tau} - i\lambda_- B_1 e^{-i\lambda_-\tau} \qquad (28a)$$

$$\frac{da_2}{d\tau} = -i\lambda_+ A_2 e^{-i\lambda_+\tau} - i\lambda_- B_2 e^{-i\lambda_-\tau} , \qquad (28b)$$

we see that the explicit rates of change are given by λ_+ and λ_-. Thus the implicit changes are slow enough only if

$$\frac{d\theta}{d\tau} << \lambda_\pm . \qquad (29)$$

This inequality is called the adiabatic inequality. Its validity is required for the adiabatic principle to be successful.

Let us evaluate $\frac{d\theta}{d\tau}$ for our problem:

$$\frac{d\theta}{d\tau} = \frac{d(\sin\theta)}{d\tau}\frac{1}{\cos\theta} = \frac{d\left(\frac{1}{\Omega}\right)}{d\tau}\frac{\Omega}{\delta} = -\left(\frac{d\delta}{d\tau}\right)\frac{1}{\Omega^2} . \qquad (30)$$

If we put this result into equation 29 and remember that the eigenvalues, $\lambda_\pm$ are smaller than Ω, we find:

$$\frac{d\delta}{d\tau} << \lambda_\pm \Omega^2 << \Omega^3 . \qquad (31)$$

The relatively robust character of the adiabatic principle is shown in Figure 4. Nearly 100% excitation of electrons is possible for the case where $\delta(\tau) = .5\tau - 5$ ($d\delta/d\tau = .5$), but when $d\delta/d\tau$ is too large, as in the case where $\delta(\tau) = 2\tau - 20$ ($d\delta/d\tau = 2$), the complete excitation is unattainable. In the two examples, $d\delta/d\tau$ differ only by a factor of 4 which does not appear to be large enough for one case to satisfy Equation 31 and the other not. This result suggests that the adiabatic principle is better than it should be as a guide to the physics. It also suggests that in practice, the only thing that matters is whether $d\delta/d\tau > \Omega^3$ or $d\delta/d\tau < \Omega^3$. Complete inversion with adiabatic excitation is very useful since complete inversion is not possible in the steady excitation unless $\delta = 0$, which may be difficult to obtain experimentally. The smooth and gradual change in λ, as shown in Figure 5 in the curve $\delta(\tau) = .5\tau - 5$, as opposed to the more abrupt change in λ for $\delta(\tau) = 2\tau - 20$, is a criterion necessary for the adiabatic principle to succeed.

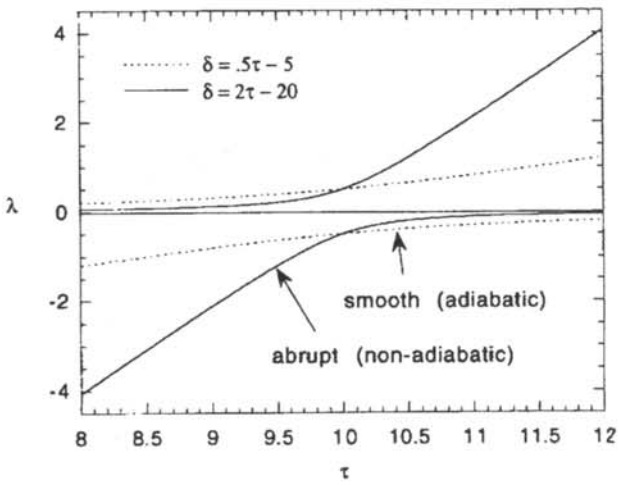

Figure 5
The two normalized eigenvalues for different rates of change of δ(τ).

ACKNOWLEDGMENTS

The author thanks Dr. Rainer Grobe for help with the mathematics. She also acknowledges the support from the Research Experiences for Undergraduates program at the Department of Physics and Astronomy of the University of Rochester, funded by the National Science Foundation.

REFERENCES

* Current address of the author: Columbia University, East Campus H202D, 411 W. 116th St., New York, NY 10027.

1. J.H. Eberly and P.W. Milonni, Encyclopedia of Physical Science and Technology, Volume 11, pp. 474-477.

FACULTY SPONSOR

Dr. J.H. Eberly
Department of Physics and Astronomy
University of Rochester
Rochester, NY 14627

SEARCH FOR PERIODIC OSCILLATIONS IN THE SOLAR CORONA

Stephen Gallo*
National Solar Observatory/Sacramento Peak
PO Box 62
Sunspot, NM 88349
received October 24, 1993

ABSTRACT

Observations of the solar corona were made for oscillations in observables such at temperature, density and velocity through spectroscopy. The green [λ5303 Å (FeXIV)] and the red [λ6374 Å (FeX)] coronal lines were analyzed. Continuous observations lasted up to 1.5 hours at a cadence of once every 24 seconds. The line profiles were calibrated with a dark and sky subtraction and fitted to a Gaussian distribution. We found possible correlation between density and temperature. There were fluctuations found in intensity (5%), velocity (1km/s) and in the Doppler temperature (10%). The power spectral analysis implies an energy flux of about 10^4 ergs/cm^2/s for frequencies of 10 mHz and below. This power may not be enough to fulfill the power requirements needed to heat the corona

INTRODUCTION

Solar oscillations in the photosphere have been studied since their discovery in 1960. [1] The amount of research on the oscillations in the solar corona, however, is considerably less. A compilation of investigations on the solar corona shows about 15 different measurements. [2] In this small sample, it is conclusive that there are oscillations in certain areas of the corona and they suggest the possibility of the oscillations being periodic. If periodic oscillations exist in the corona, they possibly could be the extensions of waves from lower levels of the sun. These oscillations could come in the form of magnetosonic waves , which propagate at an angle to the magnetic field lines, or Alfvén waves which travel solely parallel to the field lines. These waves may provide the mechanism for coronal heating.

One theoretical model suggests that Alfvén waves are amplified in certain spots in the corona, dissipating their energy primary through Joule heating. These waves tend to be found in magnetic flux tubes (localized magnetic field structures with photospheric footpoints joined by a field loop. This theory, however, has some problems. Alfvén waves are not easily excited or dissipated. The time scale of the driving force, or the period of the wave, has to be smaller than the interval it takes for the wave to traverse the loop of the tube or no excitation will occur. Granulation, convective cycling of hot gas, has a period of about 400-900 seconds, while the Alfvén wave travel time ranges from 5-300 seconds. Acoustic oscillations originating from the photosphere, or p-mode oscillations, range from 200-300 seconds, so theoretically, they can be a cause of the coronal heating. If the waves are excited, the dissipation of their energy could occur through surface waves on the skin of the loop. These waves would refract and release heat in areas of strong field gradients through Joule heating. These are very particular circumstances, so this mechanism is probably only valid for certain regions. Fortunately, this theory is reasonably well understood, as contrasted to other theories of magnetic reconnection, such as field-aligned currents and magnetohydrodynamic turbulence.

In this experiment, we observed oscillations in the gas density, the temperature and relative velocity and then searched for periodic behavior. We hoped to distinguish between magnetosonic waves and Alfvén waves through the existence of intensity fluctuations. We also hoped to establish a power limit on the waves which would be useful for evaluating theoretical models.

OBSERVATIONS

The observations were taken with the 40 cm coronagraph

Stephen is a first year graduate studeni at the Roswell Park Memorial Cancer Institute. His undergraduate degree in physics was obtained from the State University of New York at Binghamton. This research was begun during the summer of his junior year as part of a summer research internship at the National Solar Observatory. He is currently working towards a degree in biophysics.

and the Littrow spectrograph at the Evans Facility of the National Solar Observatory/Sacramento Peak. The spectra were taken with a MDA (256x403) CCD camera with a spatial resolution of 1.6 arcseconds. The observations were made in the visible range, one day in green (λ = 5303 Å) and three days in red (λ = 6374 Å). The line profile analyzed was approximately 4.9 Å in width for the green line and 8.1 Å for the red line. The observations (see Table 1) took place between March 22, 1993 and March 25, 1993, averaging 6 hours per day. All data were gathered at a height of about 60 arcseconds above the limb, or edge of the sun. This height was split up into 256 slit positions. A spectrum was taken at each slit position during an exposure time of 15 seconds with an extra 9 seconds for overhead. The typical continuous run time was between 1 and 1.5 hours, with interruptions between runs of up to an hour.

DATA REDUCTION

The CCD images were calibrated by subtracting the nonuniform thermal excitation image (dark current). The bias voltage was also subtracted our during the dark subtraction. Flatfielding, correcting for the spatial inhomogeneity of the CCD sensivity, was not done due to the lack of good flats; the calibration lamp did not illuminate the camera uniformly. The intensity error due to interference of reflected light in the camera was about 3%, not including error due to dust.

In the first line profile analysis, we fit only the central emission curve to a 2nd order polynomial. In the second method, the whole line profile and continuum were fit. In the green wavelength profile, absorption lines may skew the fit and alter the information extracted from this fit. Consequently, a point-by-point sky subtraction was used to reduce the absorption line contribution. Since the last few slit positions looked at just the sky spectra, the average intensity, $I_{sky}(\lambda,t)$ over these profiles for each wavelength and time was taken. We also found the average intensity over a small band of wavelengths in the continuum at each slit position and time, $N(x,t)$. The final subtraction resulted in an intensity for the line $I(\lambda,x,t)$:

$$I(\lambda,x,t) = I_{obs}(\lambda,x,t) - I_{sky}\,N(x,t) \qquad (1)$$

where x denotes the slit position, $I_{obs}(\lambda)$ is an observed spectral profile.

Table1 — List of Observations

Date	Hours		λ	Where	Position Angle	Comments
22 March 93	18.47	19.61	5303 Å	NW limb	281	Spatial drift
"	19.82	20.30	"	"	"	Spatial drift
"	21.03	22.17	"	"	"	Bad..Clouds
"	23.34	24.48	"	"	"	Cloudy
23 March 93	22.01	23.16	6374 Å	NW limb	281	Weak emission
"	23.54	24.39	"	"	"	Bad..Clouds
24 March 93	17.85	19.01	6374 Å	NE limb	60	Spatial Drift
"	19.85	21.01	"	"	"	Telescope moved
"	21.34	22.50	"	"	"	Bad..Cloudy
25 March 93	17.31	22.82	6371 Å			Flats..Darks

Table 1
Summary of data taken.

The data were fit to:

$$F(x) = A(0)\exp\left(\frac{-z^2}{2}\right) + A(3) + A(4)\,x + A(5)\,x^2 \qquad (2)$$

where $A(0)$ is the peak height, $A(1)$ is the center of the peak, $A(2)$ is the width of the peak, $z = (x - A(1)/A(2))$, and $A(3)$, $A(4)$ and $A(5)$ are constant to fit the continuum intensity background. The parameters A came from the best guess of a program called "Gaussfit" created in IDL™, Interactive Data Language from RSI Corporation. These parameters were then sent to a program called "Curfit" [3]. Curfit is a method of linearizing the fitting function and then applying least squares fit to the function. It then reiterates this process until the χ^2 changes by only 0.1% After fitting a spectrum with a Gaussian shape shown in Equation 2, three parameters are obtained: the height $A(0)$, the width $A(1)$ and the center of the Gaussian emission line $A(3)$.

The shift in the wavelength of the center of the emission line was transformed into velocity using the Doppler shift equation:

$$\frac{\Delta\lambda}{\lambda} = \frac{\Delta V}{c} \qquad (3)$$

where V is the velocity of the ions emitting the wavelength. Positive velocities are red shifted and negative velocities are blue shifted. The width of the Gaussian profile of the emission line can be correlated with the temperature of the emitting ions in optically thin regions. This width has both thermal and a non-thermal contributions given by: [4]

$$\frac{\Delta\lambda_d}{2\sqrt{\ln 2}} = \frac{\lambda}{c}\left(\frac{2kT}{m} + V\right)^{\frac{1}{2}} = C\,T_d^{\frac{1}{2}} \qquad (4)$$

where k is the Boltzman constant, $\Delta\lambda_d$ is the "Doppler half width" and T_d is the Doppler temperature. Hence, the parameters $A(1)$, $A(2)$ and $A(3)$ can be correlated with intensity, Doppler width temperature and Doppler velocity respectively.

The error observed in the intensity of ±3%. The error in the other parameters was determined through a computer simulation. The errors in velocity and width are strong functions of the signal to noise ratio (S/N). Our S/N ratio was defined as the height of the emission peak divided by the continuum noise. For these parameters, S/N was measured for each spatial position and time and used to compute the standard deviations in velocity and width. Figure 1 shows the error bars on the velocity measurements.

ANALYSIS

For the limited coronal region along the line of sight, the intensity, I_λ, is related to the density of the emitting ions, N_{Fe}, by: [4]

$$I_\lambda = \frac{hc}{4\pi}\,\frac{A_{ul}}{\lambda}\,\frac{N_{Fe}}{N_H}\,\frac{N_H}{N_e}\,N_e^{avg}\;f(N_e^{avg})\;g(T_e^{avg})\;l_{eff} \qquad (5)$$

Where A_{ul} is the transition probability for spontaneous emission between upper energy level u and lower energy

level l, N_e is the electron density, T_e is the electron temperature, l_{eff} is the effective path length, N_H is the hydrogen density and f and g are functions weakly dependent on electron density and temperature. For a particular wavelength λ, Equation 5 becomes:

$$I_\lambda = C\,(N_{Fe})\left[\frac{N_e^{avg}}{N_e}\, f(N_e^{avg})\, g(T_e^{avg})\, l_{eff}\right] \qquad (6)$$

where C is constant whose value is dependent upon which wavelength is picked. The factors in the square brackets in Equation 6 (besides f and g) are geometric, making the intensity essentially proportional to the density of iron ions, so:

$$\Delta I_\lambda = \Delta N_{Fe} \qquad (7)$$

DISCUSSION

The only data that was consistent upon analysis were the 22 March and 24 March data. In the 24 March data, there were well formed loop structures, one in the first half of the data and two in the second half of the data as seen in Figure 2. We consequently analyzed the 24 March data in two separate parts.

Three kinds of plots of the data were produced: the time plot for each observable; scatter plots of various combinations of observables; and power spectra, plots of the Fourier transform against the frequency. The scatter plots compared two observables against each other. The power spectra were calculated for velocity, intensity and Doppler temperatures averaged over spatial regions.

The time plots of the red line single loop show maximum variations in intensity of (5±3)%. These values are larger than most observations. Only one has shown a variation of 6%.[4] The velocity showed a (0.8±0.4)km/s variation which is a little slower than past observations. The temperature (Doppler width) exhibited a (10.0±2.5)%

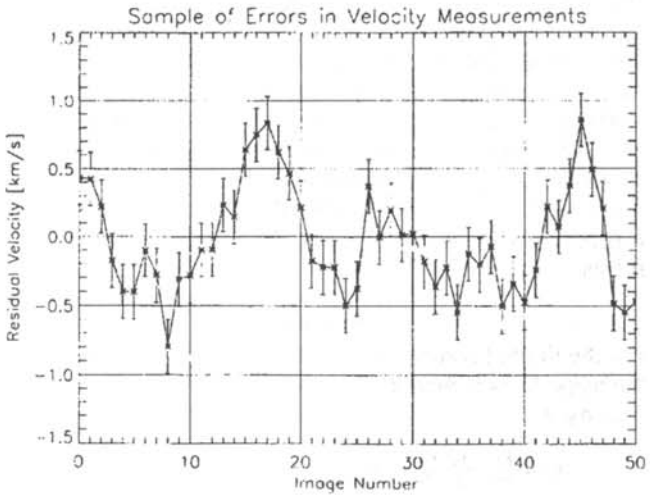

Figure 1
Velocity measuremnts with error bars.

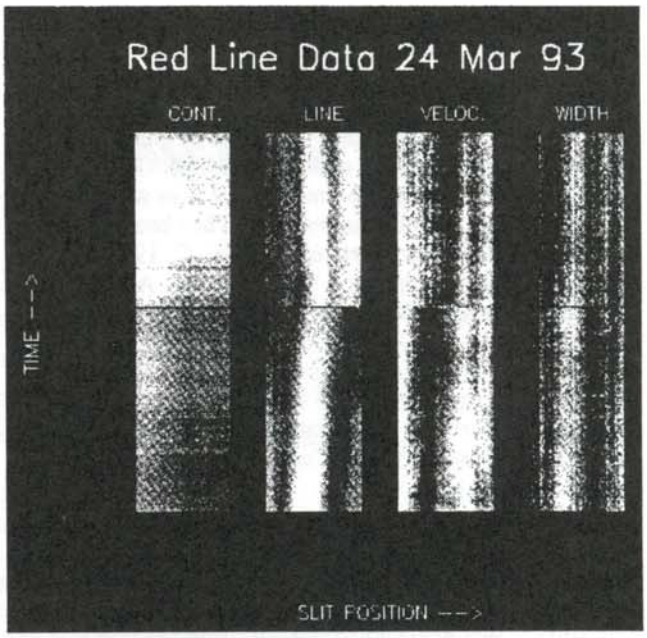

Figure 2
The red line data over time and spatial position. Notice the correlation between peak intensity and line width. The velocity has a loop like structure to it corresponding to the bright region in intensity.

variation which is similar to what has been seen before. The scatterplots made of the green line data showed random distributions in the intensity vs temperature and velocity vs temperature plots. However, there was a linear correlation between intensity and temperature. This linear relation was also found in the 24 March single loop in the red line data. This data also showed a strong correlation between intensity and velocity, but the velocity vs temperature plot was a random distribution.

Figures 3 - 5 show the results of the spectral analysis, which are mirrored about the Nyquist frequency of 22 mHz. The power spectra of the velocity plots of the red line data of the single loop show low frequency power of 16±1 (km/s)^2/Hz at 3 mHz and 13±1 (km/s)^{2}Hz at 5 mHz. The power spectra of the intensity plots shows peaks of 0.031±0.003 $(\Delta I/I)^2$/Hz at 5.5 mHz, 0.017±0.003 $(\Delta I/I)^2$/Hz at 6.5 mHz and 0.016±0.003 $(\Delta I/I)^2$/Hz at 12 mHz. The power spectra of the temperature plot showed a peak of 0.20±0.05 $(\Delta T/T)^2$/Hz at 3.5 mHz. None of these peaks overlapped. In other observations, the noise level was larger than the power peaks of the first red line data. The problems of noise in the data stemmed mostly from the short exposure time of 15 seconds. This was not long enough to collect sufficient photons to produce a good signal. The S/N for the data was about 8 - 20, which is relatively bad.

If we make some assumptions about the Alfvén waves, we can convert the power spectra's limits to ergs/cm^2/sec. Our data gives a value of about 10^4 ergs/cm^2/sec. Theo-

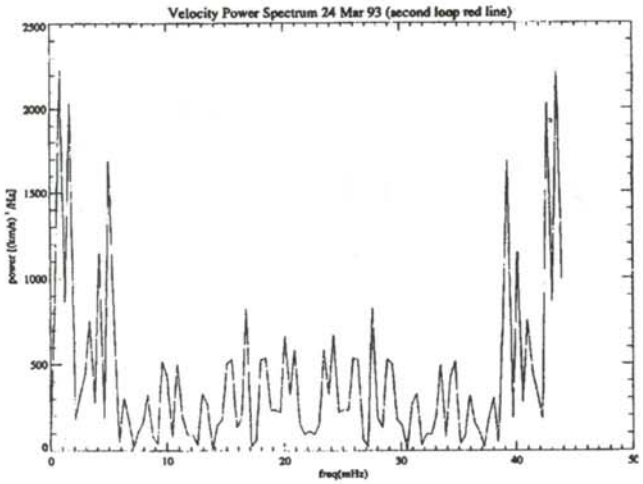

Figure 3
Velocity power spectrum in the single loop red line. Notice the peaks at 3.0 mHz and 5.5 mHz.

retical calculations for an active corona give values of 10^7 ergs/cm^2/sec.

Our data seem to confirm the existence of magnetosonic waves in the corona. These waves can not heat the corona themselves and, therefore, must act in conjunction with some other mechanism. If other waves exist, they may do so only in specific coronal locations to maintain the temperature inhomogeneity that we see. [2] It is also possible that if more than one loop exists, they may destructively interfere with each other, making oscillatory motion difficult to observe. We believe that our methods are an improvement over previous attempts to detect the waves. The data obtained in this experiment were survey data, the quality was not very good. The observations need to be taken during a more active period with longer

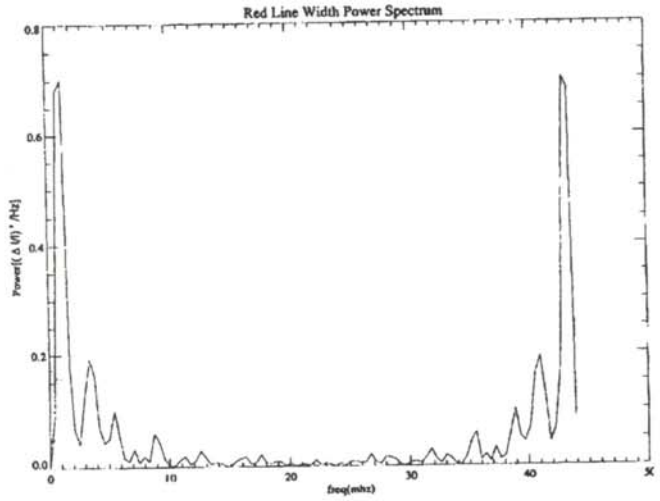

Figure 4
Power spectrum of the Doppler width temperature of the single loop red line. Notice the peaks at 3.5 mHz and at 5.5 mHz.

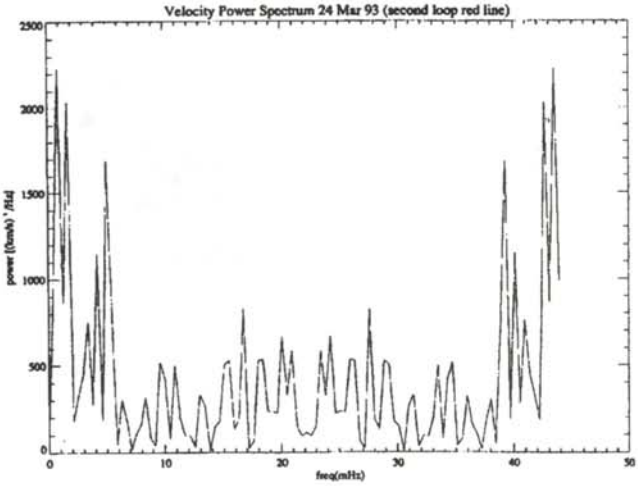

Figure 5
Velocity power spectrum in the double loop red line. Notice that the noise power is more than 100 times greater than in the single loop red line data, limiting the usefulness of these observations.

exposure times and a good seeing day.

ACKNOWLEDGMENTS

The author wishes to thank Robert J. Rutten, Jack Zirker and others on the staff of NSO/Sac for their help.

REFERENCES

* Current address of author: Biophysics, Roswell Park Cancer Institute, Elm & Carlton Streets, Buffalo, NY 14263
1. R. Leighton, R. Noyes and G. Simon, Astrophys. J., 135, (1962), p. 474.
2. T. Tsubaki, Sacramento Peak Summer Symposium, 140, (1987).
3. P.R. Bevington, Data Reduction and Error Analysis for the Physical Sciences, McGraw-Hill Book Co., New York, (1962).
4. T. Tsubaki, et. al., Solar Physics, 43, (1975), p. 147.
5. J.B. Zirker, Solar Physics, 93, (1984), p. 67.

FACULTY SPONSOR

Dr. Matthew Penn
National Solar Observatory
Sacramento Peak
P.O. Box 62
Sunspot, NM 88349

The Journal of Undergraduate Research in Physics

The Journal of Undergraduate Research in Physics is the journal of Sigma Pi Sigma and the Society of Physics Students. It is published by the Physics Department of Guilford College, Greensboro NC 27410. Inquiries about the journal should be sent to the editorial office.

The Journal of Undergraduate Research in Physics

Editorial Office -
The Journal of Undergraduate Research in Physics
Physics Department
Guilford College
Greensboro, NC 27410
910-316-2279 (voice)
910-316-2951 (FAX)

Editor -
Dr. Rexford E. Adelberger
Professor of Physics
Physics Department
Guilford College
Greensboro, NC 27410
ADELBERGERRE@RASCAL.GUILFORD.EDU

The Society of Physics Students

National Office -
Dr. Dwight Neuenschwander, Director
Ms. Sonja Lopez, SPS Supervisor
Society of Physics Students
American Institute of Physics
1 Physics Ellipse
College Park, MD 20740
301-209-3007

President of the Society -
Dr. Fred Domann
Department of Physics
University of Wisconsin at Platteville

President of Sigma Pi Sigma -
Dr. Jean Krisch
Department of Physics
University of Michigan, Ann Arbor